Accepted to ApJ: 17 January 2013
Preprint typeset using LaTeX style emulateapj v. 08/22/09

ENHANCED WARM H_2 EMISSION IN THE COMPACT GROUP MID-INFRARED "GREEN VALLEY"

M.E. Cluver[1,2], P.N. Appleton[3], P. Ogle[1], T.H. Jarrett[4], J. Rasmussen[5], U. Lisenfeld[6], P. Guillard[1], L. Verdes-Montenegro[7], R. Antonucci[8], T. Bitsakis[9], V. Charmandaris[9,10,11], F. Boulanger[12], E. Egami[13], C.K. Xu[2], M.S. Yun[14]

Accepted to ApJ: 17 January 2013

ABSTRACT

We present results from a *Spitzer*, mid-infrared spectroscopy study of a sample of 74 galaxies located in 23 Hickson Compact Groups, chosen to be at a dynamically-active stage of H I depletion. We find evidence for enhanced warm H_2 emission (i.e. above that associated with UV excitation in star-forming regions) in 14 galaxies (∼20%), with 8 galaxies having extreme values of L(H_2 S(0)-S(3))/L(7.7μm PAH), in excess of 0.07. Such emission has been seen previously in the compact group HCG 92 (Stephan's Quintet), and was shown to be associated with the dissipation of mechanical energy associated with a large-scale shock caused when one group member collided, at high velocity, with tidal debris in the intragroup medium. Similarly, shock excitation or turbulent heating is likely responsible for the enhanced H_2 emission in the compact group galaxies, since other sources of heating (UV or X-ray excitation from star formation or AGN) are insufficient to account for the observed emission. The group galaxies fall predominantly in a region of mid-infrared color-color space identified by previous studies as being connected to rapid transformations in HCG galaxy evolution. Furthermore, the majority of H_2-enhanced galaxies lie in the optical "green valley" between the blue cloud and red-sequence, and are primarily early-type disk systems. We suggest that H_2-enhanced systems may represent a specific phase in the evolution of galaxies in dense environments and provide new insight into mechanisms which transform galaxies onto the optical red sequence.

Subject headings: galaxies: groups : general – galaxies: evolution – galaxies: interactions – galaxies: ISM – galaxies: intergalactic medium – infrared: galaxies

1. INTRODUCTION

Compact Groups are key laboratories for studying morphological transformations as they represent the highest density enhancements outside of clusters, and their relatively low velocity dispersions prolong gravitational interactions (Hickson et al. 1992). Disentangling the mechanisms that influence galaxy evolution are made more challenging with growing evidence that cluster galaxies have been "pre-processed" in groups, and then subsequently assimilated into larger systems (e.g. Cortese et al. 2006). Simulations show that spirals in a group environment are strongly influenced by repetitive slow encounters, building bulge mass as gas is funnelled into the central regions, transforming them into S0 galaxies with young, metal-rich stellar populations in their inner bulges (Bekki & Couch 2011). In addition, galaxy interactions in groups may differ from isolated binary interactions because they can exhibit a broader range of behaviours, including tidal stripping and interactions with the intra-group medium (IGM; see e.g. Allen & Sullivan 1980).

Hickson (1982) identified a uniform sample of 100 nearby compact groups (Hickson Compact Groups; hereafter HCG) using the Palomar Sky Survey, and applied the criterion of 4 or more members within a 3 magnitude range (δm_B) that also satisfied an isolation constraint. These groups have been the subject of extensive follow-up and study. Radial velocities (Hickson et al. 1992) have led to the identification of true associations of galaxies, with 92 groups consisting of at least three accordant members. That many of the groups are real physical associations is further attested by the presence of hot intragroup gas in many of them (Ponman et al. 1996; Desjardins et al. 2012). Signs of interactions within these groups include peculiar rotation curves and disturbed morphologies of group members (Rubin et al. 1991; Mendes de Oliveira & Hickson 1994), as well as the presence of intragroup light (Da Rocha et al. 2008).

H I deficiency in compact group galaxies has long been suspected (Williams & Rood 1987; Huchtmeier 1997)

[1] Spitzer Science Center, IPAC, California Institute of Technology, Pasadena, CA 91125, USA
[2] ARC Super Science Fellow, Australian Astronomical Observatory, PO Box 915, North Ryde, NSW 1670, Australia
[3] NASA Herschel S Center, California Institute of Technology, Pasadena, CA 91125, USA
[4] Department of Astronomy, University of Cape Town, Private Bag X3, Rondebosch, 7701, South Africa
[5] Dark Cosmology Centre, Niels Bohr Institute, University of Copenhagen, Juliane Maries Vej 30, DK-2100 Copenhagen, Denmark
[6] Departmento de Fìsica Teórica y del Cosmos, Facultad de Ciencias, Universidad de Granada, Spain
[7] Instituto de Astrofísica de Andalucía (IAA/CSIC), Apdo. 3004, 18080 Granada, Spain
[8] University of California Santa Barbara, Department of Physics, Santa Barbara, CA 93106, USA
[9] Department of Physics, University of Crete, GR-71003, Heraklion, Greece
[10] IESL/Foundation for Research & Technology-Hellas, GR-71110, Heraklion, Greece
[11] Chercheur Associé, Observatoire de Paris, F-75014, Paris, France
[12] Institute d'Astrophysique Spatiale, Universite Paris Sud 11, Orsay, France
[13] Steward Observatory, University of Arizona, 933 N. Cherry Avenue, Tucson, AZ 85721, USA
[14] Department of Astronomy, University of Massachusetts, Amherst, MA 01003, USA

and the H I study of 72 HCGs led Verdes-Montenegro et al. (2001) to propose an evolutionary sequence in which compact group galaxies become increasingly deficient in neutral hydrogen. Multiple tidal interactions, and possible gas stripping (via interaction with the IGM) may be the cause of the observed H I depletion. More recent observations using the Green Bank Telescope, sensitive to extended, faint H I emission, have revealed a diffuse H I component in all the groups studied (Borthakur et al. 2010), explaining in part the "missing H I" reported by Verdes-Montenegro et al. (2001). Groups containing galaxies with the largest H I deficiencies are found to have a more massive diffuse-H I component (Borthakur et al. 2010). These observations have led to the conclusion that H I-deficient group galaxies lose H I into the IGM, primarily through tidal interactions. In the most evolved groups, gravitational heating may eventually create a hot X-ray emitting medium (see Ponman et al. 1996; Desjardins et al. 2012).

Leon et al. (1998) observed that galaxies located in the most compact groups within their sample of 45 HCGs have more molecular gas concentrated in their nuclei, as expected from the effects of tidal forcing within the disk. However, the link between molecular gas and star formation properties in these interacting systems is less obvious. Studies of far-infrared and CO emission of galaxies in HCGs indicate no enhanced star formation, but 20% of spiral galaxies are tentatively found to be deficient in CO emission compared to isolated and weakly interaction systems (Verdes-Montenegro et al. 1998). A recent, more extensive CO study of HCGs finds that the specific star formation rate (SFR per unit stellar mass or sSFR) is lower in H I- and CO-deficient (as compared to isolated systems) HCG galaxies, but that the star formation efficiency (SFR per unit cold H_2 mass) in these galaxies appears unaffected (Martínez-Badenes 2012).

The question of whether galaxies are stripped by interaction with a dense medium, or by tidal forces, still remains unclear. X-ray observations of 8 HCGs by Rasmussen et al. (2008) showed no obvious correlation between the presence of detectable hot intragroup gas and H I deficiency. Furthermore, in groups where X-ray emitting gas was strongly detected, it was shown that it was not of sufficient density to significantly strip H I from the group members, thus calling into question whether gas stripping by a hot X-ray medium is a viable stripping mechanism within compact groups.

Observations in the infrared with the *Spitzer* Space Telescope have led to potentially new evidence of evolutionary effects in HCGs. Johnson et al. (2007) observe a correlation in the IRAC color-color diagram of HCG galaxies, and argue for an evolutionary sequence – from groups dominated by dusty spirals with "red" IRAC colors, to groups containing evolved stellar-dominated galaxies with "blue" IRAC colors. These colors appear to correlate with the degree of H I depletion, supporting the idea of group evolution. Johnson et al. (2007) discuss a "gap" in the IRAC colour space between dusty/gas-rich and gas-poor galaxies; this apparent absence of intermediate mid-infrared colours suggests a rapid evolution from gas-rich to H I-depleted systems (Walker et al. 2010). The role of environment is further investigated in Walker et al. (2012) using a sample of 49 compact groups. They find a statistically significant deficit of galaxies in the gap region with similarities to that found for the Coma Infall region. Accelerated transformation, possibly preceded by enhanced star formation in some galaxies, is also suggested by the significant bimodality in specific star formation rate (sSFR) seen in the HCG sample of Tzanavaris et al. (2010).

Bitsakis et al. (2011) performed a UV to mid-infrared analysis of a sample of 32 Hickson Compact Groups and find that dynamically "old" groups (containing >25% early-type galaxies) are more compact and display higher velocity dispersions compared to dynamically "young" systems (containing >75% late-type galaxies). Late-type galaxies in dynamically old groups are found, on average, to have higher stellar mass and lower sSFR, attributed to a faster build in stellar mass due to past interactions compared to the dynamically young groups. Their study also finds that the majority (73%) of compact group galaxies lie in either the optical "green valley" or the "red sequence", as defined by their NUV−r colors. More than half of the early-type galaxies in dynamically "old" groups were found to be located in the "green valley" and these are predominantly (>70%) S0/SB0's.

The AGN (Active Galactic Nuclei) activity of galaxies in HCGs are a key consideration; although 46% of the sample of Bitsakis et al. (2011) have optically identified AGN, from nuclear spectra, they find no evidence of enhanced AGN activity at any stage of group evolution. This is consistent with the findings of Martínez et al. (2010) where the median HCG AGN luminosity corresponds to a low luminosity AGN (LLAGN), likely caused by gas depletion resulting in relatively low accretion rates, and also Rasmussen et al. (2008), where the frequency and strength of nuclear X-ray activity in 8 groups showed no clear correlation with the dynamical state of the group, as measured by either diffuse X-ray emission or H I-deficiency.

Our current paper is motivated by a possible new diagnostic of HCG evolution which uses mid-infrared spectroscopy from the *Spitzer* Space Telescope as a probe of the warm molecular gas in galaxies. Our team (Appleton et al. 2006; Cluver et al. 2010) discovered powerful ($L_{H_2} > 10^{35}$ W) mid-infrared molecular hydrogem (H_2) line emission from an intergalactic shock wave in Stephan's Quintet (SQ; HCG 92). The emission was found to be spatially associated with a 40 kpc-long X-ray and radio-continuum filament believed to be formed as a result of a high-speed collision (~ 1000 km s^{-1}) between a group member and tidal debris from a previous encounter within the group. In this case, the high power of the H_2 relative to both the infrared continuum and very faint PAH (polycyclic aromatic hydrocarbon) emission, and the close association with a known group-wide shock wave, makes a strong case for shock-heating as a viable mechanism in that compact group (Appleton et al. 2006; Cluver et al. 2010). Models demonstrate that driving a shock into a multi-phase medium, such as a pre-existing H I tidal arm are capable of explaining many of the observed properties of the warm H_2 emission in SQ (Guillard et al. 2009). The group members are known to be H I and CO depleted (see Yun et al. 1997; Gao & Xu 2000), and may be one of the best candidates for hydrodynamic stripping effects as much of the molecular gas appears to reside in the IGM (Guillard et al. 2012a)

based on deep IRAM CO observations. The discovery of H I and molecular gas between galaxies in HCG 92, as well as in the tidal bridge between the Taffy galaxies (Peterson et al. 2012) – a system which has recently experienced a head-on collision similar to those expected in dense environments – led to our present study of a much larger sample of 23 HCGs with *Spitzer*.

The discovery of a class of powerful H_2-emitting radio galaxies, with similar *Spitzer* IRS spectra to SQ, led to the coining of the term MOHEG (MOlecular Hydrogen Emission-line Galaxies) and are defined as having large H_2 to 7.7μm PAH emission ratios, $\geq$ 0.04, indicating excitation above that expected from UV heating (Ogle et al. 2010).

In this paper we focus on the excited H_2 properties of a sample of 74 HCG galaxies, in particular those that show H_2-enhancement as defined for a MOHEG. A subsequent paper will focus on the cold molecular gas properties of H_2-enhanced systems through IRAM CO observations and comparisons of the cold versus warm H_2 masses (and temperatures of the excited H_2). The paper is organised as follows: in Section 2 we outline the sample chosen for this study, in Section 3 we summarise the observations and data reduction procedures, and in Section 4 present results of the excited H_2 line emission survey. Section 5 explores potential sources of H_2 excitation and in Section 6 we discuss possible links to evolution within compact groups. Section 7 presents our discussion, with conclusions summarised in Section 8. Throughout this paper we assume a cosmology with Hubble constant $H_o = 73\,\mathrm{km\,s^{-1}Mpc^{-1}}$, matter density parameter $\Omega = 0.3$, and dark energy density $\Omega_\Lambda = 0.7$.

2. THE SAMPLE

We have selected 23 compact groups from the HCG catalog of Hickson (1982), representing 25% of the physically associated groups, as targets for probing active transformation. The aim of the project was to search for evidence of extended molecular hydrogen emission by selecting compact groups with intermediate H I deficiencies (like SQ) which were reasoned more likely to be in an active phase of gas stripping.

The sample of compact groups studied by Verdes-Montenegro et al. (2001) contained 72 groups with H I deficiencies ranging from -0.8 < log $[M(H\,I)_{pred}]-\log [M(H\,I)_{obs}]$ < 1.56. From this list, we selected galaxy groups with an "intermediate HI deficiency" i.e. defined as having deficiencies in the range 0 < $\log[M(H\,I)_{pred}]-\log[M(H\,I)_{obs}]$ < 0.9. This resulted in 50 out of 72 groups with a median H I deficiency of 0.48, which is close to the value of 0.49 for Stephan's Quintet. We note that the median deficiency for the full (original) sample is 0.27. However, as shown by Verdes-Montenegro et al. (2001), the spread in the distribution is quite large, and our sample selection has resulted in effectively clipping the extreme ends of the distribution for all groups. The term "intermediate H I depletion" should therefore be seen in that context. In order to form a practical sample for observation with the IRS on *Spitzer*, and to further maximize the chances of finding dynamically active systems like Stephan's Quintet, we only considered those groups that showed visible signs of tidal interaction, specifically disturbed optical disks and tidal tails, in two or more members. This resulted in 20 groups. We added an extra group, HCG 40, on the grounds that its X-ray morphology was quite similar to that of Stephan's Quintet, although its H I deficiency is higher ($\log [M(H\,I)_{pred}]-\log [M(H\,I)_{obs}$ =0.97) than most of the groups selected. In addition we added HCG 55 and 75 as groups with close associations that contain signatures of interaction. The final sample of 23 groups is listed in Table 1; galaxies that are not group members (i.e. with discordant redshifts) are indicated and not included in this analysis.

TABLE 1: HCG Sample

Group	z^a	H I Deficiency^b	Galaxies Sampled	Designation^c
HCG 6	0.0379	0.33	4	A, B, C, D$^\diamond$
HCG 8	0.0545	> 0.04	3	A, C, D
HCG 15	0.0228	0.62	3	A, C, D
HCG 25	0.0212	0.26	4	B, C†, D, F
HCG 31	0.0135	0.18	2	A+C$^\bullet$, B
HCG 40	0.0223	0.97	4	A, B, C, D
HCG 44	0.0046	0.69	3	A, B, D
HCG 47	0.0317	0.28	3	A, B, D
HCG 54	0.0049	0.49	3	A, B, C
HCG 55	0.0526	–	5	A, B, C, D, E†
HCG 56	0.0270	0.73	4	B, C, D*, E
HCG 57	0.0304	0.86	5	A, B, C$^\diamond$, D$^\diamond$, E
HCG 62	0.0137	> 0.46	3	A, B, C
HCG 67	0.0245	0.27	3	A, B, D$^\diamond$
HCG 68	0.0080	0.48	3	A, B, C
HCG 75	0.0416	–	4	A, C, D$^\diamond$, E
HCG 79	0.0145	0.41	4	A, B, C, E†
HCG 82	0.0362	> 0.76	3	A, B, C
HCG 91	0.0238	0.24	3	A, C, D
HCG 95	0.0396	> 0.21	3	A, B‡, C
HCG 96	0.0292	> 0.17	3	A, B, C
HCG 97	0.0218	0.89	3	A, C, D
HCG 100	0.0170	0.5	3	A, B, C

[a] From NED
[b] $\log[M(H\,I)_{pred}]-\log[M(H\,I)_{obs}]$; Verdes-Montenegro et al. (2001)
[c] From Hickson (1982)
† Discordant redshift (from Hickson et al. 1992)
‡ Discordant redshift (from Iglesias-Páramo & Vílchez 1998)
• Merging Object (Gallagher et al. 2010)
⋆ SL coverage only
◇ LL coverage only

Although our primary selection criterion is based on the groups exhibiting intermediate H I-depletion (based on the original definition of Verdes-Montenegro et al. 2001), the sample spans a large range of galaxy properties shared by the more complete samples of HCG groups (e.g. Bitsakis et al. 2011; Walker et al. 2012). As shown in the IRAC color-color diagram ($\log[f_{8.0\mu m}/f_{4.5\mu m}]$ vs $\log[f_{5.8\mu m}/f_{3.6\mu m}]$; Figure 1a), the intermediate H I-depletion in these groups is not biased towards mid-infrared blue or red populations, but rather spans the entire range of mid-infrared colour seen in the studies of Bitsakis et al. (2011) and Walker et al. (2012).

This color-color space has been shown to separate late-type, star-forming galaxies (top right) from early-type galaxies (bottom left). The dashed box shows the under-populated region found in the smaller sample of HCGs studied by Johnson et al. (2007) and Walker et al.

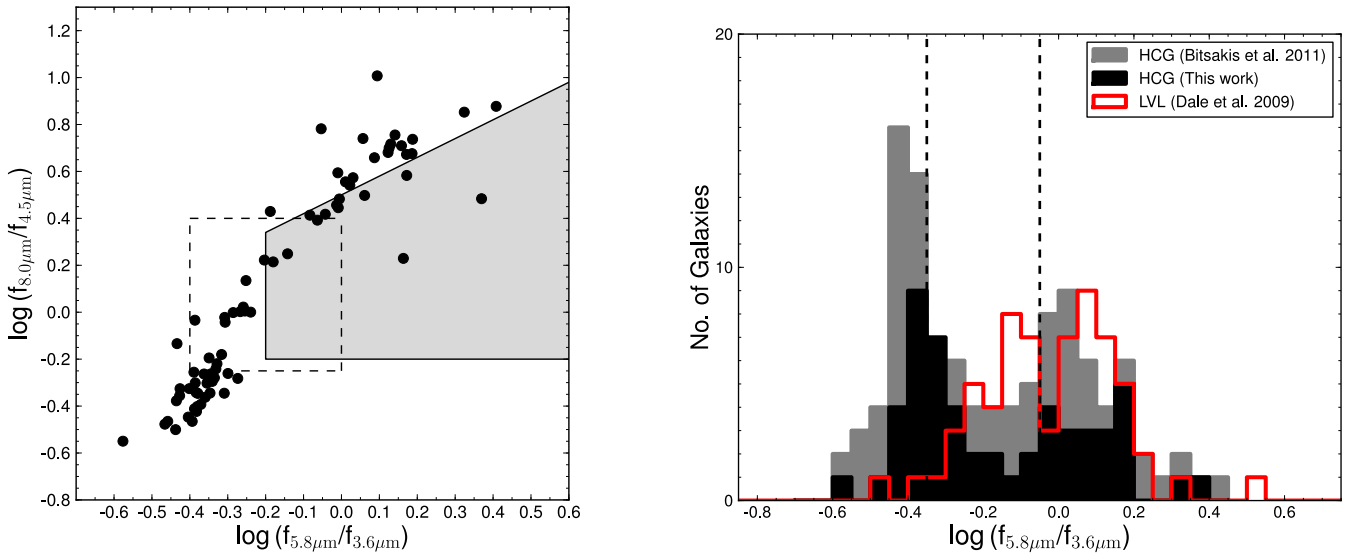

(a) (b)

FIG. 1: a) The IRAC color-color diagram of the galaxies in our sample showing the mid-infrared colours of the chiefly intermediate H I-deficiency groups. The shaded grey region indicates the AGN locus, as defined by Lacy et al. (2004), and the black dashed region shows the Johnson et al. (2007) "gap" region. b) A histogram comparing the IRAC [$f_{5.8\mu m}/f_{3.6\mu m}$] colors within our sample (black filled; $z < 0.035$ galaxies only to avoid colors affected by redshifted spectral features), versus the larger HCG sample of Bitsakis et al. (2011, grey filled; also excluding galaxies at $z > 0.035$), as well as the distribution from the Local Volume Limited (LVL) sample of nearby galaxies of (Dale et al. 2009, red unfilled) after applying a luminosity cut (see text). The black dashed lines indicate galaxies with intermediate mid-infrared colours, as determined from the distribution of Bitsakis et al. (2011).

(2010). Bitsakis et al. (2011) observe a similar lowering of density of galaxies with intermediate mid-infrared colors; they attribute this distribution to the natural result of morphological transformation as galaxies evolve from star forming to passively evolving systems. We will show later in this paper that galaxies which fall within this intermediate region of mid-infrared color preferentially show signs of shocked molecular hydrogen emission. This may support the idea that the "gap galaxies" represent a transitional population.

The mid-infrared color properties of our sample, both in the context of the larger HCG group population and local galaxy populations, is shown in Fig. 1b. Here we compare the IRAC colors of our intermediate H I-deficient sample, to the larger Bitsakis et al. (2011) HCG sample of 32 groups which was not selected for deficiency. Also shown are galaxies taken from the Local Volume-Limited (LVL) sample of Dale et al. (2009), as a comparison "field" control sample. The LVL sample consists of 256 galaxies within 11 Mpc and is dominated by spirals and irregulars; we apply a luminosity cut (as motivated by Walker et al. 2012) of $\log(L_{4.5\mu m}[erg/s/Hz]) > 27.5$ to compare galaxies with similar characteristics, which leaves 65 galaxies. As expected from the morphology-density relation (e.g. Dressler 1980), the LVL field sample contains very few early-type systems.

By comparison to the LVL sample, HCG group galaxies appear to have a well-defined red and blue sequence in this color space, with a deficiency of galaxies at intermediate color not seen in the volume-limited sample of nearby galaxies, i.e. between

$$-0.35 \leq \log f_{5.8\mu m}/f_{3.6\mu m} \leq -0.05, \quad (1)$$

This deficiency, although not a complete "gap", is what led Walker et al. (2010) to suggest HCG galaxies rapidly evolved through this intermediate color region.

3. OBSERVATIONS AND DATA REDUCTION

3.1. *Spitzer IRS Spectroscopy*

The galaxies and groups listed in Table 1 were targeted by the *Spitzer* IRS instrument (Houck et al. 2004) using the low-resolution Short-Low ($R \sim 60-127$; $5.2-14.5$ μm) and Long-Low ($R \sim 57-126$; $14.0-38.0$ μm) modules. Observations were carried out as part of GO-5 PID 50764 and taken between 2008, June 29 and 2009, January 19.

Since it was not known apriori where in the group environment shock-excited H_2 emission may be located, the primary observations employed a sparse mapping strategy – centering a 3-leg grid[15] on the most disturbed member of the group (see Figure 2). The scale was adjusted for each group to provide good coverage of the inner group in both modules. The typical coverage was linear ∼70 kpc for SL and ∼180 kpc for LL. In addition, a further two member galaxies were targeted in IRS "Staring Mode", where the target center is placed at the $\frac{1}{3}$ and $\frac{2}{3}$ position along the length of the slit. Because of

[15] In most cases this was a 2×3 sparse map with typical step sizes of 30″ parallel (to the slit) steps and 35″ perpendicular for SL, and 70″ and 35″ parallel and perpendicular in the LL module.

the way the IRS performs a staring mode observation (by sampling first the 2nd order spectrum followed by a similar observation in first order), this increases the coverage of the group, providing further information about potential extended emission in the groups, as well as often intersecting by chance (depending on the roll-angle of the focal plane at the time of the observations) additional group members. As a result, the SL and LL slits typically sampled $\sim$800 kpc^2 and $\sim$6000 kpc^2, respectively, covering the IGM and the galaxies themselves.

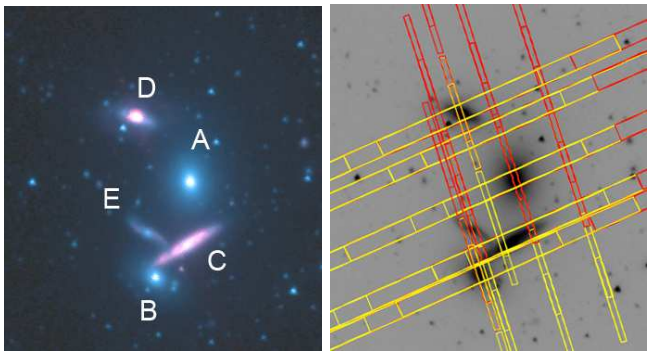

FIG. 2: The IRS sampling (Long-Low; $\sim$ 10.5″ and Short-Low; $\sim$ 3.6″ slits) shown on HCG 40 (IRAC four-color image of $\sim 4' \times 4'$). 1st order spectral coverage is shown in yellow with 2nd order in red. It should be noted the mapping combined with staring strategy probes the intragroup region, as well as the galaxies themselves.

Primary data reductions were performed by the *Spitzer* Science Center (SSC) pipeline, version S18.0.2-18.7.0, which performs standard spectral reductions such as wavelength and flux calibration, ramp fitting, dark current subtraction and detector droop and non-linearity linearity corrections. Basic Calibrated Data (BCDs) frames, output from the pipeline, were combined within the SSC tool CUBISM (Smith et al. 2007a), optimised for extended sources, with each AOR forming one spectral cube. This was done to ensure proper background subtraction, using backgrounds taken close in time to the observations. This was achieved using either dedicated backgrounds or from the "off" position BCDs with coverage outside of the group.

Pixel outlier rejection was done using the CUBISM algorithm (with a conservative 8σ clipping) and then by visual inspection of the spectral cubes to ensure that no weak signals are lost. The cubes were inspected for any H_2 emission in the IGM and spectra extracted for each galaxy with coverage. Since we are particularly interested in emission from the disk, we were careful to extract spectra along the slit with an aperture large enough to capture most of the source's light while still maximising the signal to noise of the spectrum. Extraction areas for SL and LL for each galaxy are listed in Table A5. Due to the coverage obtained through the sparse mapping mode, several galaxies have "off-nuclear" coverage where the slits have not been centred on the nucleus; these are indicated in Table A5 and are treated as separate spectra to those that cover the nuclear region.

Spectra were extracted for all but 4 galaxies in the sample (HCG 6A, 6C, 6D and 79C) where no signal above the noise was detected. Spectra were converted to flux densities (mJy) using the extraction areas, and SL scaled to LL to match continuum levels in cases that required it (see Table A5). This accounts for beam resolution differences between the long and short order; here we make the assumption that the emission in each slit is uniform. The scaling of spectra is further discussed in Section A of the Appendix.

PAHFIT was used to characterize our spectra, but each visually inspected one by one to determine which lines were detected reliably and which were marginal detections ($<2.5\sigma$). PAHFIT is a spectral decomposition package (Smith et al. 2007b) that fits emission lines, bands and dust continua to stitched LL and SL spectra.

The spectra RMS (root mean square) for determining upper limits were measured using ISO Spectral Analysis Package (ISAP)[16].

3.2. *Spitzer IRAC and MIPS Photometry*

The *Spitzer* IRAC (Fazio et al. 2004) and MIPS (Rieke et al. 2004) instruments were used to obtain imaging at 3.6, 4.5, 5.8 and 8.0μm, and 24μm, respectively, of our sample and observed as part of PID 50764 (P.I. Appleton), PID 40459 (P.I. Le Floc'h), PID 631 (P.I. Mazzarella) and PID 101 (P.I. Kennicutt).

IRAC photometric measurements (to obtain colours) for 21 galaxies in our sample are taken from Bitsakis et al. (2011) as indicated in Table A1. Fluxes for the remainder of galaxies were carefully measured to improve the deblending systematics where contamination from nearby stars and galaxies may affect the photometry. For these systems, the data was reduced using the SSC science pipeline version S18.5.0 and 18.7.0. Galaxy photometry was performed using a matched elliptical aperture, determined by the 1σ isophote in IRAC 3.6μm, after foreground contaminating stars were masked from all images and replaced by the corresponding isophotal value of the source. Nearby contaminating galaxies were similarly masked. The local background was determined from the median pixel value distribution within a surrounding annulus. Aperture corrections were applied as specified by the IRAC Handbook. The formal photometric uncertainties are $\sim$5% for the IRAC calibration error.

Potentially saturated sources, particularly in IRAC 3.6μm and 4.5μm, namely HCG 56B, 91A, 96A and 100A were investigated. HCG 96A was saturated in the cBCDs at IRAC 3.6μm, 4.5μm and 5.8μm. For this system the 1.2 s HDR (High Dynamic Range) exposures were used to determine the IRAC fluxes. For HCG 100A the source counts for all bands was nominal, although at the full well capacity. For 56B and 91A the source counts for IRAC 5.8μm and 8.0μm were nominal and below the saturation limit at 3.6μm and 4.5μm. However, since the peak pixel flux is within the non-linear regime at 3.6μm and 4.5μm, the integrated fluxes may be slightly underestimated (as indicated in Table A1), but the mid-infrared colors are likely unaffected.

[16] The ISO Spectral Analysis Package (ISAP) is a joint development by the LWS and SWS Instrument Teams and Data Centers. Contributing institutes are CESR, IAS, IPAC, MPE, RAL and SRON.

For galaxies located at $z > 0.035$ the shifting emission features, in particular the 6.2μm PAH, affect the observed colours of a galaxy. For the groups in our sample affected by this (HCG 6, 8, 55, 75, 82 and 95) we have corrected the IRAC fluxes for redshift (i.e. "k-corrected") using the empirical template library from M. Brown et al. (in prep.). Consisting of 125 galaxy templates of local, well-studied and morphologically diverse galaxies (e.g. SINGS, the *Spitzer* Infrared Nearby Galaxy Survey), these are generated using optical and *Spitzer* spectroscopy with matched aperture photometry from *GALEX*, *XMM* UV, SDSS, 2MASS, *Spitzer* and WISE, synthesized with MAGPHYS (da Cunha et al. 2008). For galaxies with recessional velocities $< 9000\,\mathrm{km\,s^{-1}}$, k-corrections do not appreciably affect the mid-infrared colours, or analysis derived thereof, presented in this work.

MIPS 24μm data was processed through SSC science pipeline versions 18.1.0, 18.12.0 and 18.13.0, achieving a spatial resolution of $\sim$6″. The LL spectral extraction areas output from CUBISM were used to make matched aperture photometric measurements using the IRAF[17] task, POLYPHOT. For star-forming and AGN-dominated spectra showing continua with a strong power-law dependence, we applied colour corrections as recommended in the MIPS Handbook. This correction is of the order of $\sim$5%. The MIPS calibration error is of the order of $\sim$10 – 20%. .

In the cases of 31AC, 40C, 44A and 75D we have H_2 detections in LL coverage without matching SL coverage. In order to measure the 7.7μm PAH emission, we use the prescription of Helou et al. (2004) and measured matched (to the LL extraction) apertures of the IRAC 3.6μm and IRAC 8μm bands. By subtracting a scaled version of IRAC 3.6μm from IRAC 8μm we can compensate for stellar light contamination and use this as a measure of the strength of the aromatic emission within the band (see, for example, Roussel et al. 2007). This was also done for the IGM detections discussed in Section 4.1.1.

4. RESULTS

4.1. *Emission from Warm Molecular Hydrogen*

The pure rotational transitions of molecular hydrogen covered by the IRS SL and LL spectral windows at the redshifts of the HCGs, are the 0-0 S(0), S(1), S(2), S(3), S(4) and S(5) lines at 28.22, 17.03, 12.28, 9.67, 8.03 and 6.91μm, respectively. These can be excited in a variety of astrophysical processes including, UV pumping and collisional heating in photodissociation regions associated with star formation (e.g. Hollenbach & Tielens 1997), X-ray heating in XDRs (X-ray dominated regions) particularly those associated with AGN (e.g. Draine & Woods 1992), cosmic ray heating (e.g. Dalgarno et al. 1999) and heating by turbulence or shocks (e.g. Shull & Hollenbach 1978). We detect ($> 2\sigma$) two or more lines of warm H_2 in 32/74 galaxies in our sample; this includes marginal detections (i.e. between 2 and 3 σ), but we do not include these in the analysis that follows. In the group IGM, we find evidence of two locations with tentative detections of excited H_2 – both suffer diminished signal to noise of the S(1) line due to an artifact latent in the first set of BCDs.

Many of the galaxies located in HCGs are star forming systems, generating a UV radiation field capable of heating very small grains (VSGs) and exciting PAH molecules, thus producing distinctive dust features in the mid-infrared. We shall focus on systems where the H_2 emission is enhanced relative to UV-excitation. In order to separate mechanical heating of H_2 from UV-heating within photodissociation regions (PDRs), we use the 7.7μm PAH emission band as a discriminator (described by Ogle et al. 2010). The ratio of H_2 luminosity (summed over the $0-0\,$S(0)–S(3) lines) to the 7.7μm PAH luminosity allows us to determine which systems have enhanced H_2 relative to SINGS star-forming galaxies (Roussel et al. 2007) and thus exhibiting "MOHEG-type" emission. This value ($\geq$ 0.04) of $H_2\,$S(0)-S(3)/7.7μm PAH, hereafter referred to as H_2/7.7μm PAH for brevity, separating PDR-dominated H_2 heating from other heating sources has been demonstrated by radiation modeling (Guillard et al. 2012b).

4.1.1. *H_2 in the Group IGM*

A key aim of this project was to determine the prevalence of warm H_2 emission in the IGM of HCGs most likely to be in an active stage of transformation. From the sample of 23 groups, we have discovered two locations showing warm H_2 detections in the IGM. These are both detected in the LL spectra and appear associated with the edges of galaxy disks. Figure 3 and 4 show the detections in HCG 40 and HCG 91, respectively. We consider these preliminary, demanding follow-up observations for confirmation.

In HCG 40, we detect the S(1) line (Figure 3) outside the Sb galaxy HCG 40C (the positions of the IRS slits are shown in Fig. 2).Using the IRAC 3.6μm and 8.0μm coverage to provide an estimate of the 7.7μm PAH emission ($4.77\times10^{-16}\,\mathrm{W.m^{-2}}$) and the combined S(0) and S(1) flux of $1.02\times10^{-17}\,\mathrm{W.m^{-2}}$, we find a H_2/7.7μm PAH ratio of > 0.021. This can regarded as a lower limit due to missing SL coverage, as well as the poor signal to noise of the S(1) line due to the latent-induced flux bias in the first set of BCDs.

The VLA H I distribution (from Verdes-Montenegro et al., private communication) is shown as contours in Figure 3a and indicates the presence of H I around 40B and 40C, with a tail towards 40D. Interactions with a tidal tail could account for this emission, and would also explain the (albeit weak) warm H_2 signal from 40B presented in the next section. Follow-up IRAM CO observations (Lisenfeld et al., in prep.) find indications for extended molecular CO emission at the location of the IGM detection within the group.

In HCG 91, we find a detection at what appears to be the edge of the disk of 91A, a star-forming galaxy (Figure 4). The LL2 spectrum suffers from a similar latent effect as above (due to observing a bright target prior to this observation) and the first BCD is contaminated, resulting in a lower signal to noise for the S(1) detection, yet there is a strong S(0) detection. Moreover, the estimated H_2/7.7μm PAH ratio (calculated as above, with an H_2 flux of $1.43\times10^{-17}\,\mathrm{W.m^{-2}}$ and 7.7μm dust estimate of

[17] IRAF is distributed by the National Optical Astronomy Observatory, which is operated by the Association of Universities for Research in Astronomy, Inc., under cooperative agreement with the National Science Foundation

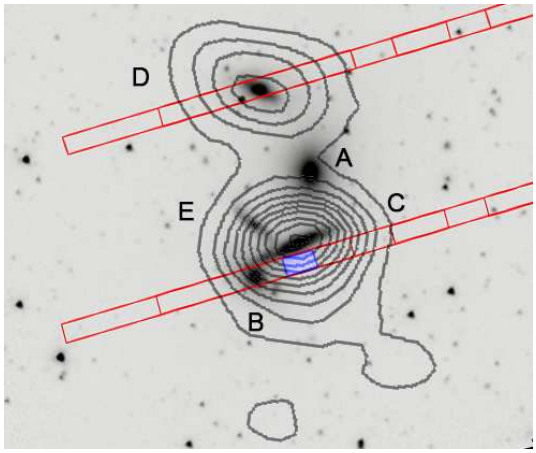

(a)

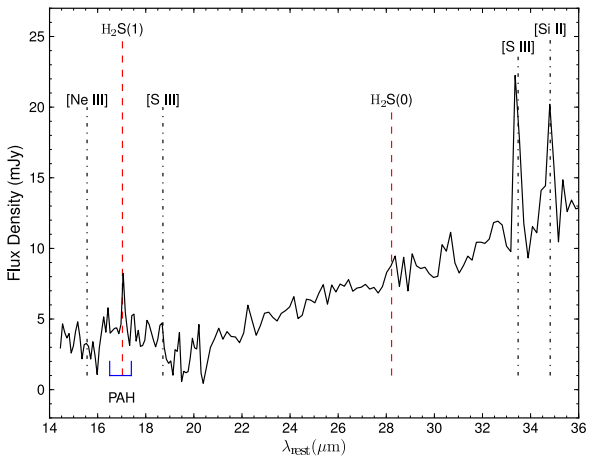

(b)

FIG. 3: a) HCG 40 IRAC 3.6μm image ($\sim$4′$\times$ 4′) with LL slit coverage overlaid; the blue box shows the position of the extraction. The VLA integrated H I distribution (Jy/beam/s) from Verdes-Montenegro et al. (private communication) is shown as overlaid contours; image reproduced with kind permission. North is up and East is left. b) LL Extraction centered on $09^{h}38^{m}53.45^{s}$, -04°51′47.2″. Due to a latent-induced flux bias in the first set of BCDs, the signal-to-noise of the S(1) line is diminished.

3.51×10^{-16} W.m^{-2}) is >0.041 and therefore would be classified as a MOHEG even without SL coverage.

Barnes & Webster (2001) find two H I knots centered around HCG 91A and 91C with a connection between the two through a gas bridge (shown as contours in Fig. 4a), since there is a common velocity between the southern part of HCG 91C and the northern part of HCG 91A. Amram et al. (2003) find that the Hα distribution shows a tidal arm pointing from HCG 91A towards HCG 91C. They also find a double gaseous component for HCG 91C strongly suggestive of a past interaction. They propose a scenario where HCG 91C is passing through the group forming the tail of HCG 91A.

The location of these two detections suggest a possible connection with disks interacting with the group IGM.

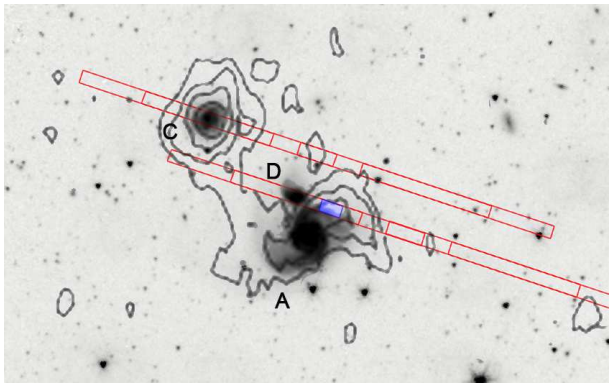

(a)

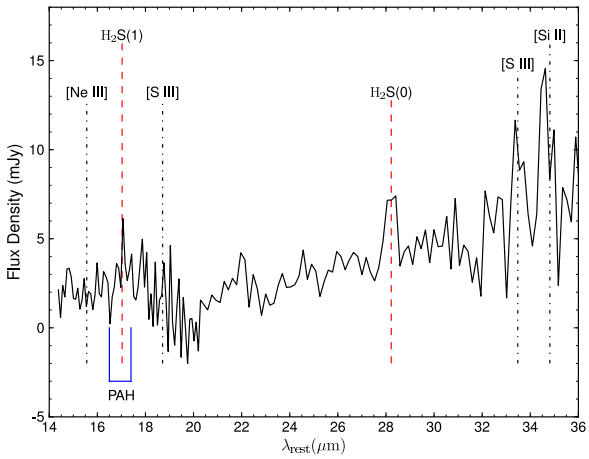

(b)

FIG. 4: a) HCG 91 IRAC 3.6μm image ($\sim$6′$\times$ 10′) with LL slit coverage overlaid; the blue box shows the position of the extraction. The ATCA H I distribution from Barnes & Webster (2001) are shown as contours. Image reproduced with kind permission from the authors. North is up and East is left. b) LL extraction centered on $22^{h}09^{m}06.20^{s}$, -27°48′09.1″. Due to a latent effect in the first set of BCDs, the signal-to-noise of the S(1) line is diminished.

4.1.2. *H_2 in Individual Group Galaxies*

The mapping strategy employed in this study resulted in 74 compact group galaxies with an IRS spectrum (either full or partial). In Table A1 of the Appendix, we indicate whether a warm H_2 detection was made in an individual galaxy. The fluxes determined for the H_2 emission lines are presented in Table A2; we note that several systems have their SL and LL lines presented separately due to the regions sampled by the IRS not overlapping (and therefore not joined together). In addition, spectra that are not centred on the nucleus (and therefore dominated by emission from the disk) are indicated. For completeness, extraction areas for H_2-detected galaxies are listed in Table A5.

The strengths of the PAH complexes and atomic emission lines for the H_2-detected systems are presented in Tables A3 and A4, respectively. Upper limits for the H_2 S(0)–S(3) emission for galaxies without H_2 detections, and measurements of their PAH features, are included in

TABLE 2: H_2-detected Galaxies: H_2 and 24μm Data

Source	H_2 S(0)–S(3) ($W\,m^{-2}$)	log $L(H_2)$ ($L_\odot$)	$H_2/7.7\mu m$[a]	$F_{24\mu m}$ mJy	log L_{24}[b] $L_\odot$
6B	1.633e-17	7.093	0.198	2.14	8.31
15A	8.012e-18	6.321	0.044	3.46	8.05
15D	2.280e-17	6.776	0.112	3.25	8.03
25B*	3.299e-18	5.883	0.098	–	
25B$^{\diamond\dagger}$	1.159e-17	6.429	–	3.08	7.95
31A+C$^\diamond$	2.004e-17	6.289	0.002	286.87	9.54
40B	5.619e-18	6.227	0.083	4.72	8.25
40C$^\diamond$	9.166e-17	7.439	0.010	46.52	9.24
40D	4.707e-17	7.150	0.013	67.71	9.40
44A$^{\diamond *}$	1.338e-16	6.355	0.027	98.74	8.32
44D	6.202e-17	6.021	0.021	35.22	7.87
47A	2.556e-17	7.181	0.035	31.96	9.38
55C	8.395e-18	7.126	0.018	5.31	9.02
56B	1.829e-17	6.885	0.053	138.52	9.86
56C	1.205e-17	6.704	0.037	[c]3.59	8.27
56D*	1.338e-17	6.749	0.018	6.03	8.50
56E	3.169e-18	6.124	0.012	4.88	8.41
57A†	2.501e-17	7.140	–	–	–
57A$^\diamond$	8.385e-17	7.665	0.174	8.52	8.77
67B	2.330e-17	6.920	0.006	20.84	8.97
68A	4.275e-17	6.228	0.741	13.63	7.83
68B	8.100e-18	5.505	0.073	6.77	7.52
68C	1.311e-16	6.714	0.044	137.13	8.83
75D$^\diamond$	9.676e-18	6.985	0.010	8.59	9.03
79A	2.693e-17	6.503	0.011	15.13	8.35
79B	1.045e-17	6.092	0.010	18.11	8.43
82B	8.947e-18	6.821	0.045	3.26	8.48
82C	5.567e-17	7.614	0.014	62.51	9.76
91A	5.931e-17	7.227	0.030	159.93	9.75
91C	1.770e-17	6.702	0.016	13.35	8.68
95C	3.354e-17	7.438	0.071	13.35	9.14
96A	8.378e-17	7.553	0.007	914.78	10.69
96C	3.928e-17	7.224	0.018	30.45	9.21
100A	5.459e-17	6.910	0.013	102.11	9.28

[a] MOHEG is assigned based on $H_2/7.7\mu m \geq 0.04$
[b] $L_{24} \equiv \nu L_\nu(24\mu m)$
* $S(2)$, $S(3)$ lines (SL coverage)
$^\diamond$ $S(0)$, $S(1)$ lines (LL coverage)
† Off nuclear extraction
* Known MOHEG from Roussel et al. (2007)
[c] Contamination from 56B and 56D

TABLE 3: Morphologies and Optical Nuclear Classifications

Galaxy	Morphology	Nuclear class. (optical)	T-Type†
MOHEGs with $-0.35 \leq \log[f_{5.8\mu m}/f_{3.6\mu m}] \leq -0.05$			
6B	S?$^\diamond$, Sab*	TO[a]	–
15A	S0$^\diamond$	dLINER[b]	-2
15D	S0$^\diamond$	LINER[b]	-3
25B	SBa*	H II[c]	-2
40B	SA0(r) pec$^\diamond$	No emission[b]	-3
44A	SA(s)a pec$^\diamond$	AGN[a]	1
56C	S0/a pec$^\diamond$	No emission[b]	0
57A	Sab? pec$^\diamond$, Sb*	AGN[a]	2
68A	S0?$^\diamond$, S0*	No emission[b]	-2
68B	S0$^\diamond$	TO[a], dLINER[b]	-2
82B	SB0?$^\diamond$, Sa*	TO[a]	-2
95C	Sm*	AGN[a]	–
MOHEGs with $\log[f_{5.8}/f_{3.6}] > -0.05$			
68C	SB(r)b$^\diamond$	TO[a], LINER[b]	3
56B‡	SB0*	AGN[a], Sy 2[b]	–
non-MOHEG H_2-galaxies			
31A+C	Sm/Im*	H II[a]	–
40C	SB(rs)b pec$^\diamond$	TO[a], H II[b]	3
40D	SB(s)0/a pec$^\diamond$	TO[a], H II[b]	0.3
44D	SB(s)c pec$^\diamond$	TO[a]	5
47A	SA(r)$^\diamond$	AGN[a]	–
55C	SBa pec?$^\diamond$, E*	–	1
56D	SA(s)0/a pec?$^\diamond$, S0*, •	TO[a], H II[b]	0
56E	SB0 pec?$^\diamond$, S0*, •	H II[a], H II?[b]	-2.1
67B	Sb$^\diamond$	H II[a]	3
75D	Sd*	H II[c]	7
79A	Sa pec$^\diamond$	TO[a], LINER[b]	1
79B	S0 pec$^\diamond$	H II?[b]	-2
82C	S?$^\diamond$, Im*	TO/AGN[a]	–
91A	SB(s)bc pec?$^\diamond$, SBc*	AGN[a]	4.3
91C	S?$^\diamond$, Sc*	–	–
96A‡	SA(r)bc pec$^\diamond$	AGN[a]	4
96C	S?$^\diamond$, Sa*	TO[a]	–
100A	S0/a$^\diamond$	TO[a]	0

TO indicates line ratio's intermediate between AGN and H II
dLINER designation indicates a LL (low luminosity) AGN
† From the RC3 Catalogue of de Vaucouleurs et al. (1992)
* From the Optical Classification of Hickson et al. (1989)
$^\diamond$ From the Classification of de Vaucouleurs et al. (1991)
• Misclassification Bitsakis et al. (2011)
‡ AGN-dominated Mid-Infrared Spectrum
[a] Optical Classification from Martínez et al. (2010)
[b] Optical Classification from Coziol et al. (2004)
[c] Optical Classification from Brinchmann et al. (2004)

the Appendix.

In Table 2 we list the summed H_2 fluxes, $H_2/7.7\mu m$ PAH ratio and MIPS 24μm fluxes (measured within a matched aperture). Upper limits and marginal detections are not included in the summed H_2 fluxes. Our sample contains 13 systems with enhanced H_2 emission, satisfying the MOHEG criteria ($H_2/7.7\mu m$ PAH ≥ 0.04); here we include HCG 56C with its $H_2/7.7\mu m$ PAH ratio of 0.037. The remaining systems (19 in total), have nominal H_2 emission, consistent with UV photoionization. There is one exception to list: HCG 44A has limited IRS coverage, rendering the $H_2/7.7\mu m$ PAH ratio as an upper limit. However, from the SINGS study, we know it has a $H_2/7.7\mu m$ PAH value of 0.042 (Roussel et al. 2007) and is therefore a weak MOHEG. We therefore include it as a MOHEG in our sample and use this value and its value of $L(H_2\,S(0)\text{-}S(3))/L_{24} = 0.022$ (Roussel et al. 2007) in future analyses.

As shown in Section 2, the distribution of Bitsakis et al. (2011) indicates a lowering in the density of galaxies, compared to the LVL galaxy colors, in the region given by Equation (1). If we separate the MOHEGs according to mid-infrared color, we find 12 located between $-0.35 \leq \log[f_{5.8\mu m}/f_{3.6\mu m}] \leq -0.05$ (i.e. intermediate mid-infrared colors); these systems have enhanced H_2 relative to their star formation, and their mid-infrared colors reflect that globally they are not dominated by star formation (or AGN emission); this is a clear indication that the warm H_2 is not UV-excited. This is discussed further in Section 4.1.4.

The morphological types of the H_2-detected systems are given in Table 3, where de Vaucouleurs et al. (1991) classifications are given for most of the sample, or Hickson et al. (1989) for those that were absent or assigned

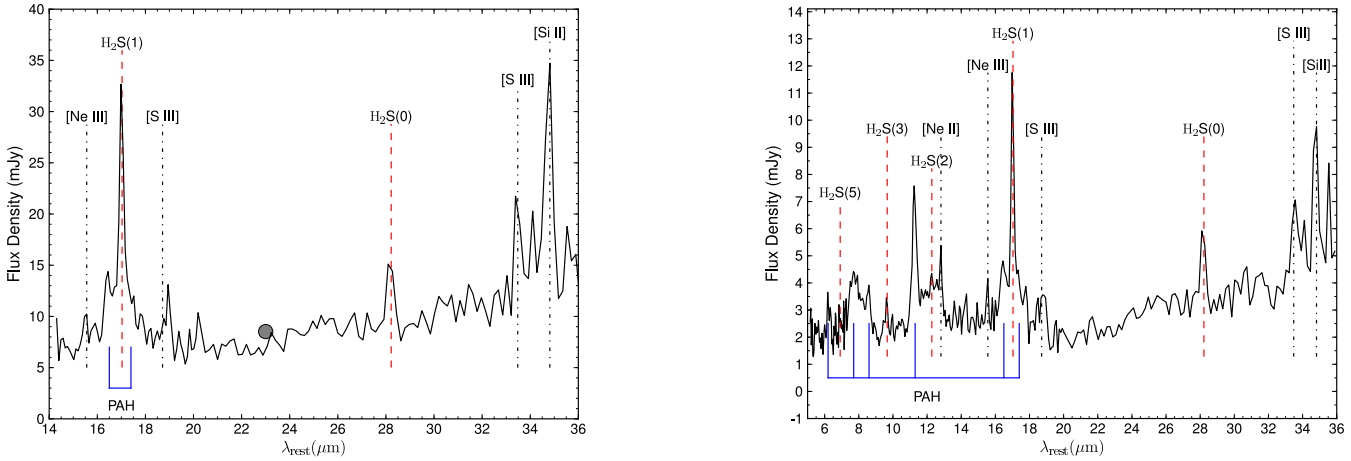

(a) HCG 57A - including the nuclear region

(b) HCG 57A - off-nuclear extraction

FIG. 5: Spectra of HCG 57A. The matched MIPS 24μm photometry is shown as a filled grey circle.

unknown classification. We include the nuclear classifications from Coziol et al. (2004), Brinchmann et al. (2004), Martínez et al. (2010), as well as the T-Type from the RC3 catalogue of de Vaucouleurs et al. (1992).

We include spectra for the non-MOHEG H_2 galaxies in Section B of the Appendix, as well as any discussion pertaining to individual systems. Spectra for the MOHEG galaxies are presented in the following section.

4.1.3. *Spectra of MOHEG Sources*

The power in the H_2 emission lines compared to the mid-infrared continuum is particularly noticeable in several MOHEGs. For example, in Figure 5 we show two spectra of HCG 57A, one centered on the nuclear region (LL only) and a matched, off-nuclear extraction in the disk of the galaxy, made possible by the sparse mapping strategy employed (see Section 3.1). The nuclear extraction shows powerful H_2 S(1) and S(0) emission and, although we have no coverage of the PAH bands, we do not see a steeply rising mid-infrared continuum typical of star-forming and AGN-dominated systems.

The off-nuclear extraction shows powerful H_2 emission with relatively weak 6.2 and 7.7μm PAH emission. This spectrum suggests a non-star-forming mechanism able to excite the H_2 in the disk of galaxy, offset from the nucleus.

In Figures 6, 7 and 8 we plot the spectra of the other HCG galaxies classified as MOHEGs that lie at intermediate mid-infrared colors (Equation 1) as used in Table 3). In particular, HCG 6B (Fig. 6a) and HCG 15D (Fig. 6c) show the distinctive H_2 S(1) emission line dominating the spectrum, with little 6.2 and 7.7μm PAH emission, reflected in Figure 11.

HCG 25B has SL coverage of the nuclear region (Fig. 6e) and we see high signal to noise H_2 S(2), S(3) and S(5) emission (the weaker S(4) transition is not seen above the PAH emission at 8μm). Similar to HCG 57A, 25B has coverage of the disk region – it covers a larger region compared to the SL extraction, and is noisier, yet we see the S(1) clearly above the weak mid-infrared continuum, again suggestive of a mechanism influencing regions away from the nucleus.

For HCG 68A and 68B (Fig. 7d and e), we see the strong contribution from the stellar continuum ($\lambda < 18\mu$m), indicative of their early type morphology (S0), yet the H_2 S(1) and S(3) ortho transitions feature strongly. The 7.7μm PAH is particularly weak in HCG 68A and only an upper limit exists. In HCG 68B the PAH is clearly defined, but the power in the H_2 lines is striking.

By contrast, the galaxy HCG 40B (Fig. 6d) has the S(1) line weakly detected with similarly low 7.7μm PAH emission. The fact that the 11.3μm PAH often features prominently in these spectra is not surprising as the large, neutral PAHs can be excited by soft radiation from evolved stars (Kaneda et al. 2008) and this would be consistent with their early-type morphologies.

In contrast to the typical MOHEG spectra presented in this paper, the MOHEG HCG 95C exhibits an exceptional, likely tidally-induced, star formation spectrum (Fig. 8). The strong PAH emission and steeply rising 24μm continuum is indicative of a system dominated by star formation. Figure 8b shows that the galaxy is highly disrupted due to an interaction with 95A, with its current state classified as an Sm morphology. Iglesias-Páramo & Vílchez (1998) find evidence for two nuclei and suggest it is either part of an ongoing merger between two galaxies, or is seen in projection with, each system having interacted with 95A individually to produce the bridges and tails. Interestingly, the mid-infrared color of 95C – after applying a k-correction – is not strongly star-forming and indeed, its $\log[f_{5.8\mu m}/f_{3.6\mu m}]$ ratio of -0.08 places it at intermediate mid-infrared color, but closest to the mid-infrared "red" population.

Finally, there are two galaxies in our sample that show MOHEG-like emission with global mid-infrared colours that suggest they are dominated by star formation, or AGN activity ($\log[f_{5.8\mu m}/f_{3.6\mu m}] > -0.05$). The spectrum of HCG 68C (Figure 9a) appears typical of a star-forming galaxy, with a steeply rising mid-infrared continuum and clear 6.2 and 7.7μm PAH emission. Whereas HCG 56B shows a distinctive AGN-dominated mid-infrared spectrum (Fig. 8b) with a substantial warm dust continuum and the high ionisation [NeV] 24.32μm

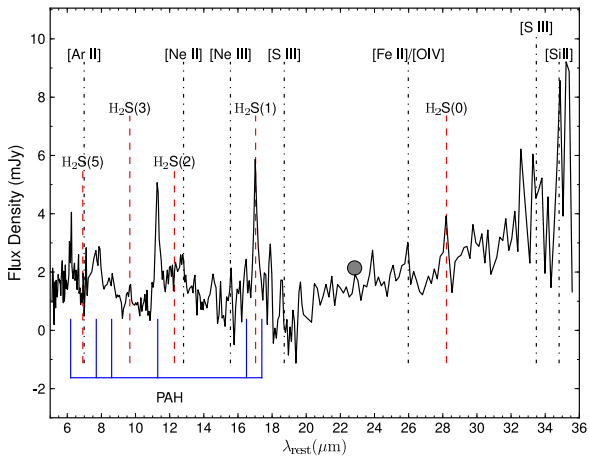

(a) HCG 6B

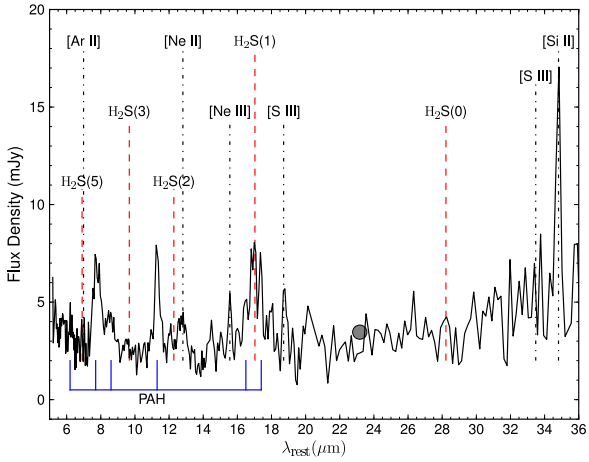

(b) HCG15A

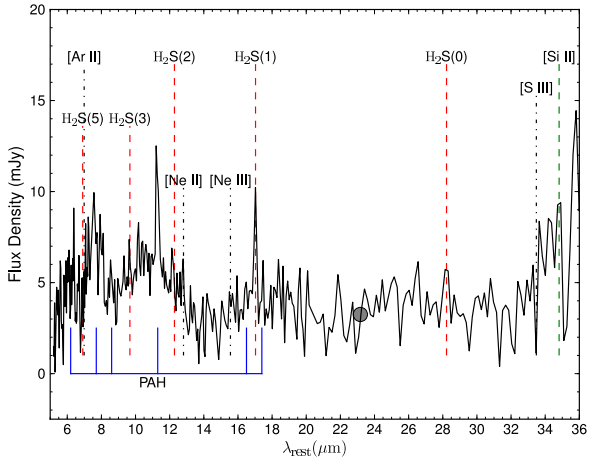

(c) HCG15D

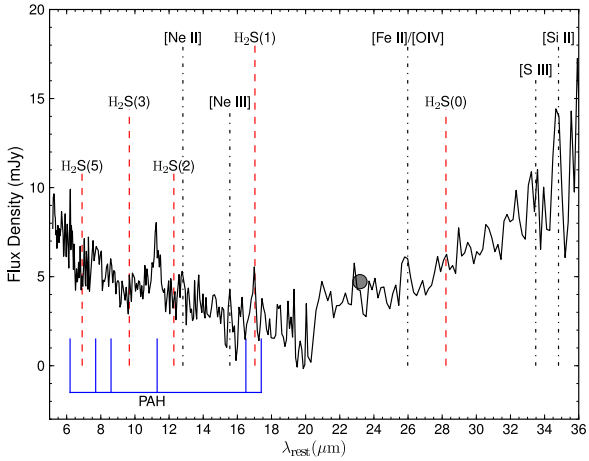

(d) HCG 40B

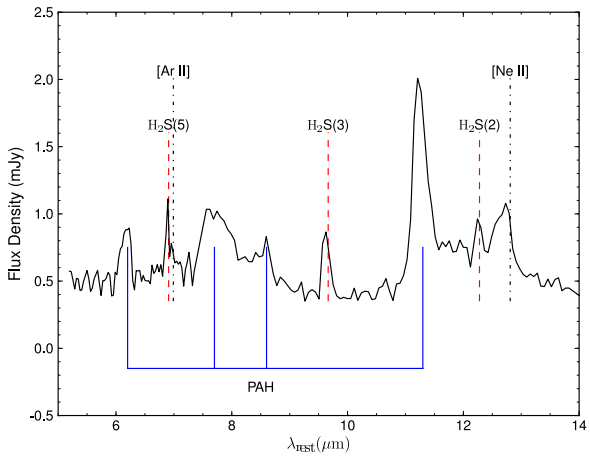

(e) HCG25B - including the nuclear region

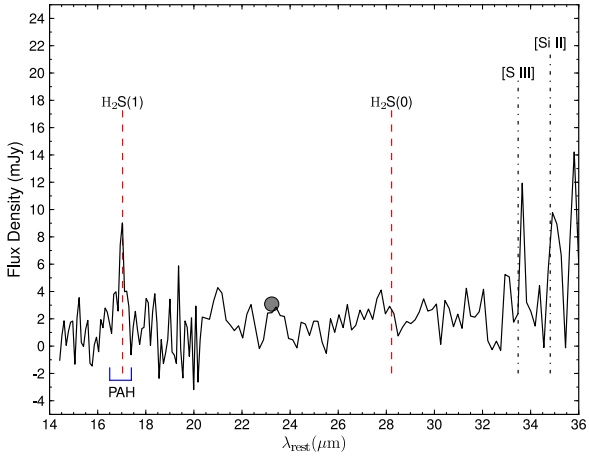

(f) HCG25B - off-nuclear extraction

FIG. 6: MOHEGs with Intermediate Mid-infrared Colours. The matched MIPS 24μm photometry is shown as a filled grey circle.

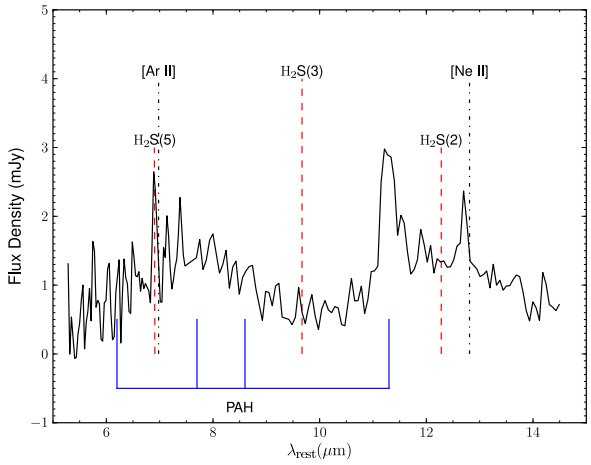

(a) HCG 44A - SL (Off-Nuclear)

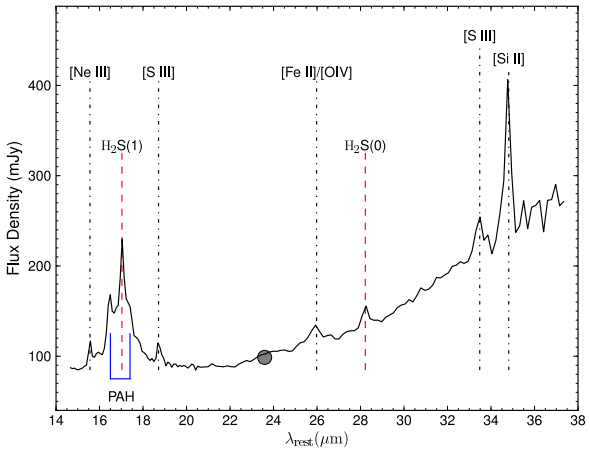

(b) HCG 44A - LL (Nuclear)

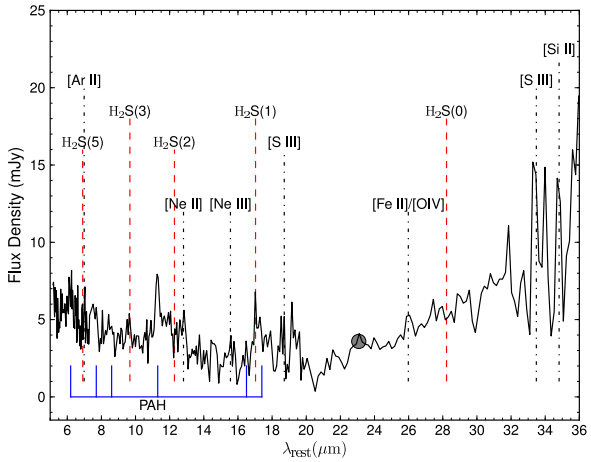

(c) HCG 56C

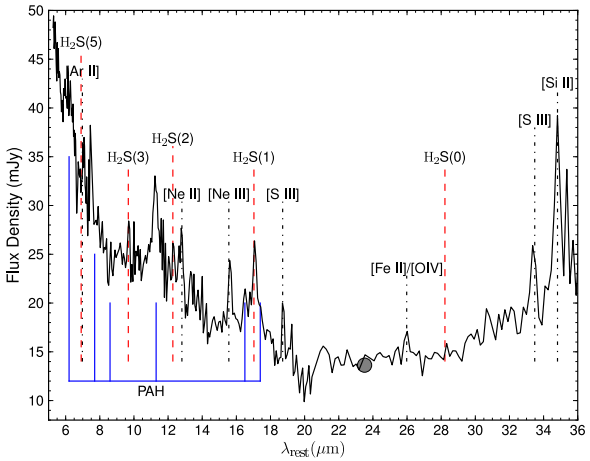

(d) HCG 68A

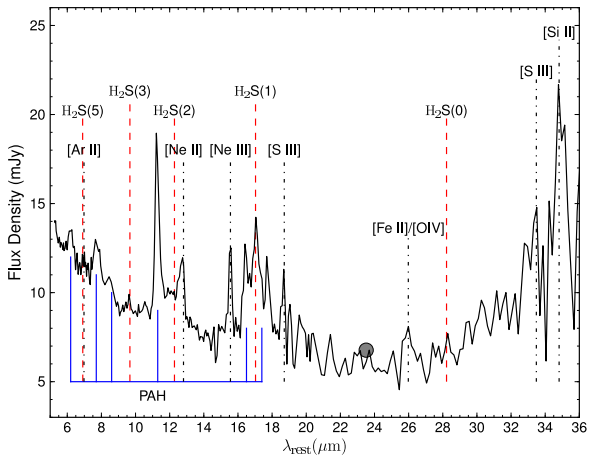

(e) HCG 68B

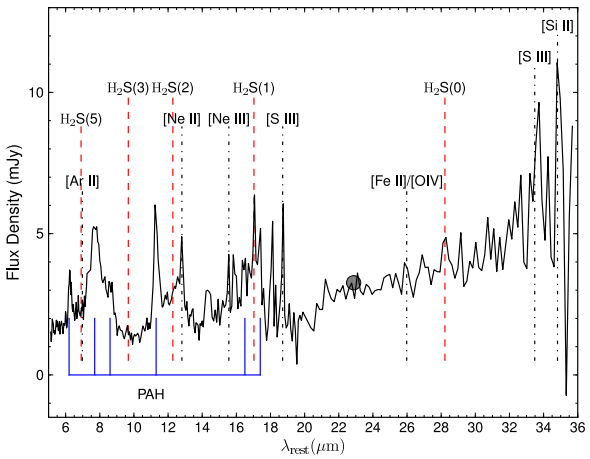

(f) HCG 82B

FIG. 7: (a)−(f) MOHEGs with Intermediate Mid-Infrared Colours; matched MIPS 24μm photometry is shown as a filled grey circle.

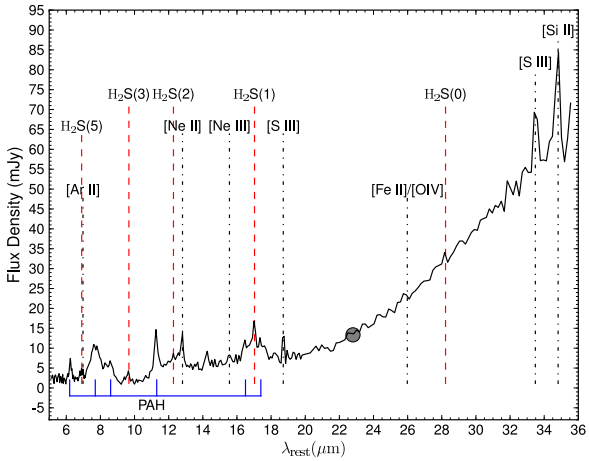

(a) HCG 95C

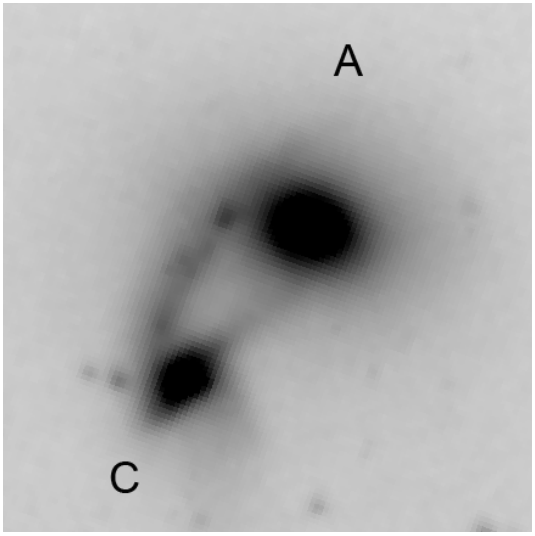

(b) HCG 95C

FIG. 8: (a) Spectrum of MOHEG HCG 95C with matched MIPS 24μm photometry shown as a filled grey circle. b) IRAC 3.6μm image of HCG 95C (field of view of $\sim$1$'\times$1$'$, North is up and East is left).

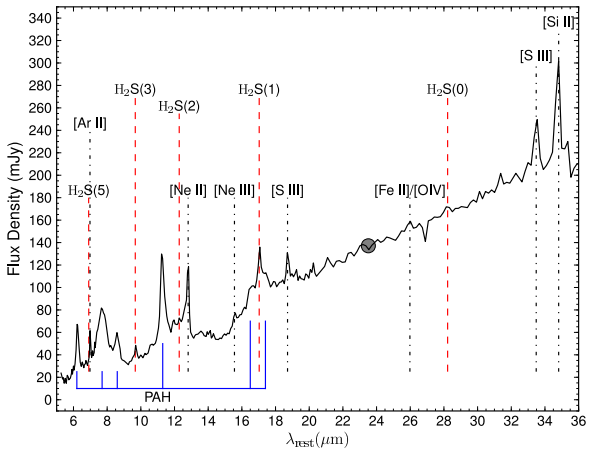

(a) HCG 68C – Star Formation-dominated spectrum

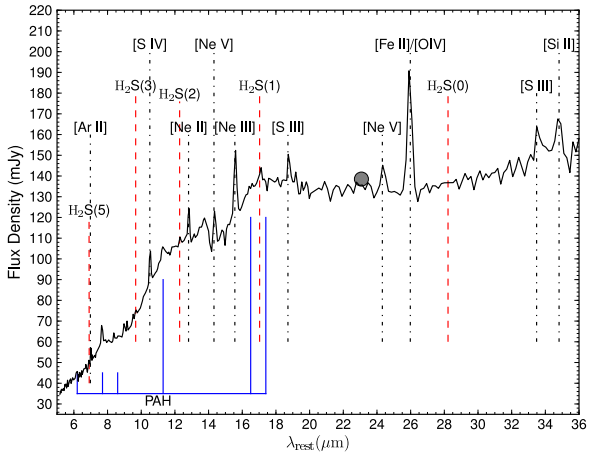

(b) HCG 56B – AGN-dominated spectrum

FIG. 9: MOHEGs with Star Formation-/AGN-Dominated Colours. The matched MIPS 24μm photometry is shown as a filled grey circle.

and [OIV] 25.89μm (blended with [FeII] 25.98μm in LL) emission lines. This galaxy is classified as a Seyfert 2 (Khachikian & Weedman 1974). Given the powerful continuum emission, the warm H_2 lines do not appear very strong, but the weak 7.7μm PAH band gives rise to a high H_2/7.7μm PAH ratio. This system may be exhibiting excited H_2 produced within an XDR associated with the AGN (Maloney et al. 1996) or, alternatively, due to jet interactions with the ISM (Ogle et al. 2010).

4.1.4. *Comparison to Mid-Infrared Color*

In Figure 10 we plot the IRAC color-color diagram ($\log[f_{8.0\mu m}/f_{4.5\mu m}]$ vs $\log[f_{5.8\mu m}/f_{3.6\mu m}]$) for our entire sample of 74 galaxies, color-coded according to their mid-infrared spectral features as follows: no warm H_2 detected (black triangles), H_2 detected in line with UV-heated PDR emission (blue circles), H_2 detected in a galaxy with an AGN-dominated mid-infrared spectrum (yellow circle), H_2-enhanced galaxies i.e. MOHEGs (green squares), and MOHEGs with AGN-dominated mid-infrared spectra (yellow squares). For reference, we include the region defined by Walker et al. (2010) as the gap in color-color space. We note that our mid-infrared spectra sample the nuclear and disk regions and reflect the galaxies' global properties – optical nuclear classifications from the literature are provided in Table 3. This is likely why several galaxies with star-forming, mid-infrared colours are not detected in H_2; a discussion of this is included in Section C of the Appendix.

For comparison, we also plot in Figure 10 the IRAC colors of the shocked region in SQ (shock sub-region; see Cluver et al. 2010) and the SQ member galaxies.

The H_2-enhanced systems (green squares) are located preferentially in and around the lower left part of the red box, which suggests a possible connection to transformation from optically blue star-forming to red sequence,

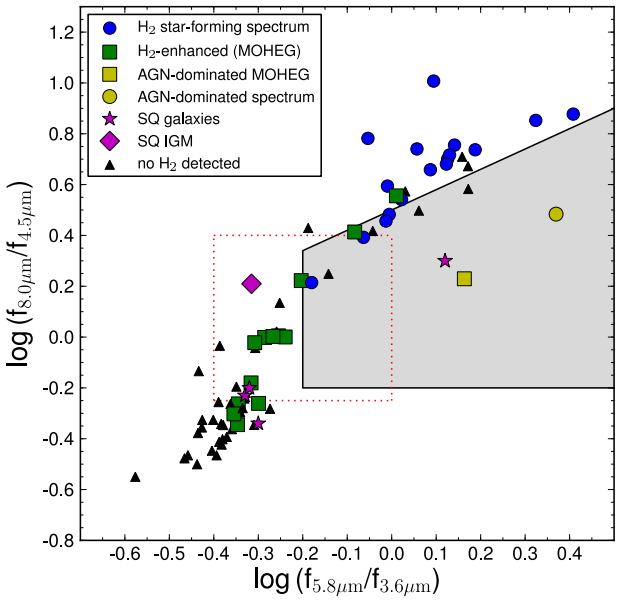

FIG. 10: IRAC colour-colour diagram for the sample; H_2-enhanced galaxies (MOHEGs) are shown as green squares, H_2-detected galaxies are shown as blue circles. The red dashed box shows the underpopulated region in color-color space from Walker et al. (2010). The shaded area corresponds to the AGN colour selection criteria of Lacy et al. (2004); AGN-dominated systems (as determined by their mid-infrared spectra) are in yellow. The purple diamond is the location of the shocked IGM in SQ (from Cluver et al. 2010), with SQ member galaxies shown as magenta stars.

passively evolving systems. To explore this further, we plot in Figure 11, the $H_2/7.7\mu$m PAH ratio as a function of mid-infrared color (*Spitzer* IRAC 5.8μm/3.6μm bands); here H_2 represents the sum of S(0)-S(3) lines, as per the definition of MOHEG, as listed in Table 2. We note that HCG 68A has an upper limit for its 7.7μm PAH detection, the other lower limits are due to not having a complete spectrum to determine the total warm H_2 emission. The dashed lines indicate the intermediate mid-infrared color space given in Equation (1) and which we shall refer to as the mid-infrared "green valley".

Apart from the AGN-dominated systems (in yellow), the $H_2/7.7\mu$m PAH ratios appear to increase towards blue IRAC color, with MOHEGs predominately found at intermediate color in what we now term the mid-infared green valley. A discussion of the link between the optical and mid-infrared green valley for HCG MOHEGs is included in Section 6.

4.1.5. *H_2 and the Mid-Infrared Continuum*

VSGs (very small grains) reprocess UV radiation to give rise to the mid-infrared continuum at 24μm. Since a UV radiation field can be produced by star formation, AGN emission and radiative shocks (Dopita & Sutherland 1996), a paucity of 24μm emission relative to warm H_2 is a strong indicator of non-radiative (e.g. shock) heating of H_2. In star-forming galaxies, $L(H_2)/L_{24}$ appears to decrease with increasing L_{24} (Roussel et al. 2007). This effect is similar to the observed decrease

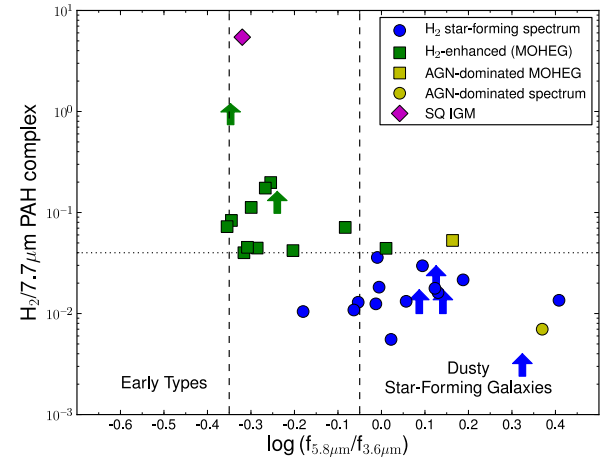

(a)

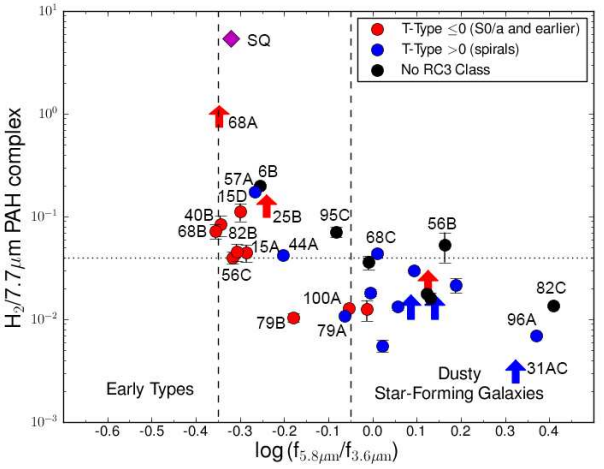

(b)

FIG. 11: a) $H_2/7.7\mu$m PAH ratio as a function of IRAC color ($f_{5.8\mu m}/f_{3.6\mu m}$) with the same symbols as in Figure 10. Lower limits are shown as arrows and the location of the IGM shock in SQ is plotted as a magenta diamond. The dashed lines indicate intermediate mid-infrared colours (determined in Section 2) and the dotted horizontal line indicates MOHEG H_2-enhancement (Ogle et al. 2010). b) $H_2/7.7\mu$m PAH ratio as a function of [$f_{5.8\mu m}/f_{3.6\mu m}$] color color-coded according to T-Type. Error bars from the combined line measurements are indicated, although for several systems they are comparable to the size of the marker.

in L(PAH)/L_{24} ratio, as L_{24} increases, seen in starbursts and ULIRGS possibly due to increasing AGN heating in these systems (e.g. Desai et al. 2007). Depletion of VSGs due to shocks may also be a factor.

We plot in Fig 12a the ratio of H_2 to 24μm luminosity as a function of log[$f_{5.8\mu m}/f_{3.6\mu m}$] color and we see a similar distribution to that of the $H_2/7.7\mu$m PAH ratio. The increased $L(H_2)/L_{24}$ values (on average) of the MOHEG systems compared to non-MOHEG star-forming systems indicates the importance of non-radiative heating, most likely due to shocks. We find that systems with AGN-dominated mid-infrared colors (HCG 56B and HCG 96A)

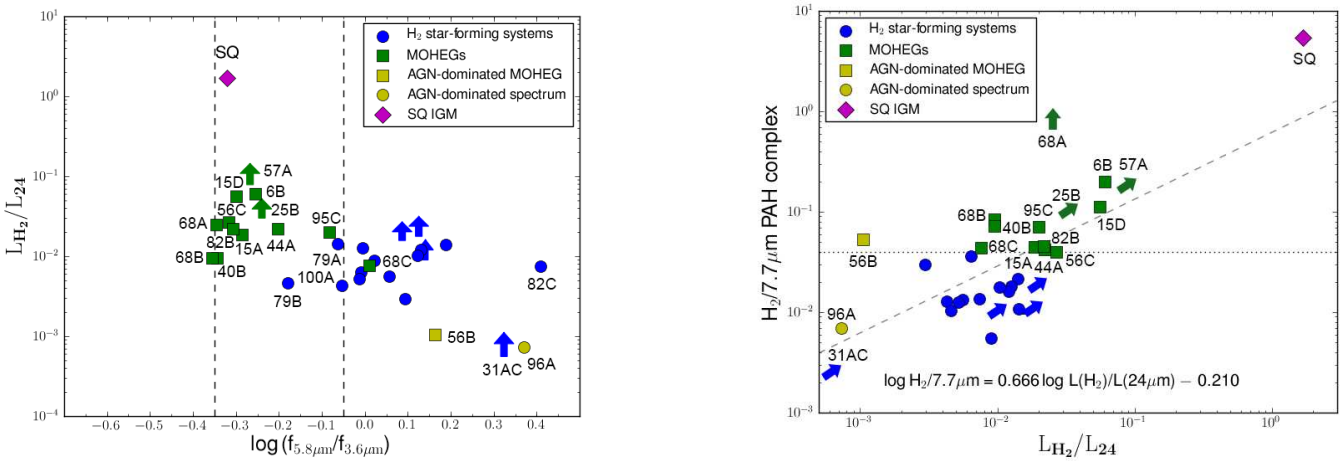

FIG. 12: a) $L_{H_2\,S(0)-S(3)}/L_{24}$ luminosity ratio for H_2-detected systems as a function of $\log[f_{5.8}/f_{3.6}]$ color with the same symbols as in Figures 10 and 11a. Arrows represent systems where the H_2 luminosity is a lower limit and the vertical dashed lines are from Equation 1. The diamond shows the location of the shocked IGM of SQ (from Cluver et al. 2010). b) $H_2/7.7\mu$m PAH ratio as a function of $L_{H_2\,S(0)-S(3)}/L_{24}$ with the same color-coding as on the left. The dotted line indicates MOHEG H_2-enhancement (Ogle et al. 2010). Arrows indicate systems with lower limits for their H_2 fluxes (due to not having the full SL+LL coverage) and are not included in the least-squares fit (grey dashed line); the best-fit relation is given at the bottom of the figure.

have low $L(H_2)/L_{24}$ values, but the highest L_{24} luminosities in the sample, lying within the locus found for radio galaxies (Ogle et al. 2010). This is in agreement with their mid-infrared spectra.

The $H_2/7.7\mu$m PAH versus $L(H_2)/L_{24}$ ratios (Fig. 12b) indicate that the 7.7μm PAH emission decreases in line with a decrease in L_{24}. Omitting lower limits and mid-infrared AGN-dominated systems, we show a least-squares fit to the data as the grey dashed line in Fig 12b. The clear outlier is HCG 56B with a large L_{24}, yet high $H_2/7.7\mu$m PAH emission indicative of MOHEG activity. The deficit of 24μm continuum relative to H_2 emission in the HCG MOHEGs (except for HCG 56B) strongly suggests shock heating.

4.2. *Atomic Emission Lines*

In this section we discuss the ionic emission of several key systems, as well as the sample overall. In Figure 13a and b we plot the $H_2/7.7\mu$m PAH ratios as functions of [NeIII] 15.56μm/[NeII] 12.81μm and [SIII] 33.48μm/[SiII] 34.82μm, respectively. We note that for the majority of HCG MOHEGs, the [NeII] 12.81μm, [NeIII] 15.56μm, [SIII] 33.48μm and [SiII] 34.82μm are upper limits or marginal detections and are not shown.

The [NeIII] 15.56μm/[NeII] 12.81μm ratios shown in Fig. 13a occupy the same range as what is found in the SINGS sample (Dale et al. 2009) and starburst systems (Bernard-Salas et al. 2009). HCG 68B and 15A have the highest ratios of [NeIII] 15.56μm/[NeII] 12.81μm (3.1 and 2.6, respectively) and are classified as low-luminosity LINERS from their optical spectra (Coziol et al. 2004). We note that 68B and 15A are NVSS catalogued radio sources (see Table D2).

HCG 68A also has a relatively high ratio, but Coziol et al. (2004) assign it as having no clear optical emission lines, however, it is an NVSS source (see Table D2). Since [NeIII] 15.56μm and [NeII] 12.81μm can also be shock-excited (Allen et al. 2008) and is observed associated with the high-velocity shock in SQ (Cluver et al. 2010) and in supernovae remnants (Neufeld et al. 2007), in the absence of an AGN [NeIII] 15.56μm and [NeII] 12.81μm emission may be arising due to shocks. HCG 56B has a similarly high [NeIII] 15.56μm/[NeII] 12.81μm ratio within this sample ($\sim$ 1.86) signifying a hard radiation field. As discussed in Section 4.1.3. it is a known Seyfert 2 galaxy.

For HCG 57A's off-nuclear extraction, the [NeIII] 15.56μm/[NeII] 12.81μm ratio is $\sim$ 0.77 indicating a radiation field typical of star-forming and Seyfert sources (Dale et al. 2006).

The nebular line [SIII] 33.48μm can be used to determine the relative enhancement of [SiII] 34.82μm, usually occurring in active galaxies with hard radiation fields, associated with XDR emission and, finally, due to shocks returning Si to the gas phase (as seen in SQ; Cluver et al. 2010). [SIII] 33.48μm/[SiII] 34.82μm ratios of between 0.5 and and 2 (Fig. 13b) are expected for star-forming regions (Dale et al. 2009), with an average of $\sim$0.8. [SIII] 33.48μm/[SiII] 34.82μm values of < 0.4 generally suggest enhanced [SiII] 34.82μm emission, indicative of the presence of an AGN or shocks. Very few HCG MOHEGS can be plotted on this figure, mostly due to the [SIII] 33.48μm line having only an upper limit (see Table A4). However, HCG 68A has a [SIII] 33.48μm/[SiII] 34.82μm value of 0.36, significantly lower than the SINGS ratios (Dale et al. 2006). This may be an indication of silicon atoms being liberated from dust grains driven by shocks. The galaxy is an NVSS source, but is not classified as an AGN optically (Coziol et al. 2004). HCG 57A's off-nuclear spectrum has a [SiII] 34.82μm/[SIII] 33.48μm of $\sim$ 1.71, which is marginally higher than the average found for typical,

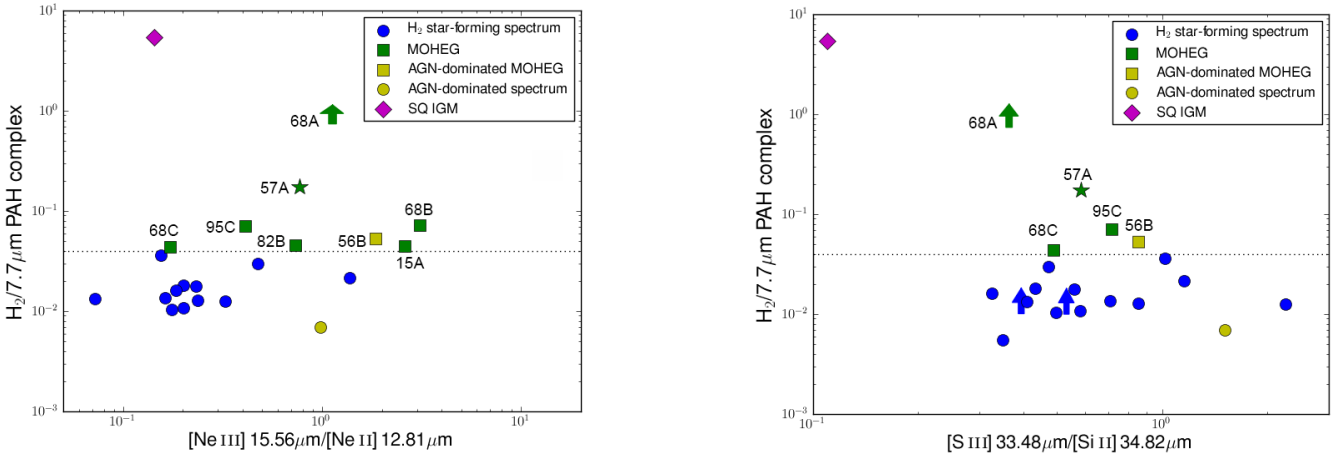

FIG. 13: a) $H_2/7.7\mu$m PAH plotted as a function of [NeIII] 15.56μm/[NeII] 12.81μm with the same color-coding as Figures 10 and 11a. The off-nuclear extraction of HCG 57A is shown as a star. b) $H_2/7.7\mu$m PAH plotted as a function of [SIII] 33.48μm/[SiII] 34.82μm with the same color designation as on the left.

star-forming galaxies ($\sim$ 1.2, Dale et al. 2006) despite not incorporating the nucleus.

5. SOURCES OF H_2 EXCITATION

5.1. *AGN and X-ray Excitation of H_2*

Studies of AGN activity with HCG galaxies have found most to be low luminosity AGNs (LLAGN; Coziol et al. 2004; Martínez et al. 2010), with a ratio of broad-to narrow-line AGNs of only 3%. As shown by Coziol et al. (2004), the LLAGN are either LINERS or Seyfert 2 systems based on their emission line diagnostics. From the optical classifications of Coziol et al. (2004) and Martínez et al. (2010) of the H_2-detected galaxies (shown in Table 3), 50% have H II classifications, 50% have a Transitional Object classification and 25% have AGN designations. Only one H_2-detected galaxy has a LINER classification (HCG 79A). By comparison, the MOHEG systems have one H II classification (HCG 25B), 29% classified as LINERs, 29% classified as Transitional Objects and 29% with AGN designations based on optical spectra of their nuclear regions. 21% of the MOHEGs have no detectable optical emission. This indicates fewer H II systems, but more LINERs objects amongst the MOHEGs compared to the H_2-detected systems, whereas optical AGN are roughly equally represented in both.

Powerful AGN in our sample, as measured by the shape of the IRS spectrum and high-excitation emission lines, are rare. Only two galaxies, HCG 56B and 96A (classified as Seyfert 2 systems optically, Coziol et al. 2004), have clear power-law, mid-infrared spectra. Tidal interactions are expected to trigger nuclear activity. However, since galaxies are being stripped, their neutral gas reservoir rapidly becomes depleted causing relatively low accretion rates onto the black hole (Martínez et al. 2010).

Ogle et al (2007; 2010) explained the powerful excited H_2 emission in their sample of 3CR radio galaxies to be the result of shocks associated with radio jets from these generally low-luminosity AGN interacting with the host galaxy (see also Guillard et al. 2012b). However, in our sample, this mechanism is unlikely (except in the case of HCG 56B) since very few are known radio sources, and those that are detected are low luminosity (see Table D2).

Molecular hydrogen can be excited directly by X-ray heating (Lepp & McCray 1983), either in the form of XDRs associated with AGN (Maloney et al. 1996), or due to the presence of hot, diffuse intragroup gas. We know from SQ that the collision of a group galaxy with previously stripped tidal material can produce hot plasma and copious X-ray emission (Trinchieri et al. 2005; Guillard et al. 2009). However, whereas the most H I-deficient systems, and therefore most dynamically evolved, would be expected to be the most X-ray luminous, half are undetected (Rasmussen et al. 2008). We present archival X-ray data of the MOHEG groups in Section D.1 and find 5 out of 8 have detections, but all with relatively low luminosities. The highest X-ray luminosity system is HCG 82 with a luminosity of 1.9×10^{42} erg s^{-1}, whereas the typical luminosity is closer to $\sim 10^{41}$ erg s^{-1}).

To investigate X-ray heating within the galaxies themselves, we use archival Chandra and *XMM* data available for 9 out of 14 MOHEGs (HCG 15A, 15D, 40B, 56B, 56C, 57A, 68A, 68B and 68C; Appendix D.2). The X-ray emission is insufficient to excite the amount of warm H_2 we observe and we conclude that it is unlikely to be a significant heating mechanism.

The available radio data (see section D.2) suggests that H_2 excitation due to cosmic rays in these systems, by analogy with SQ (Guillard et al. 2009) and the Taffy galaxies (Peterson et al. 2012), is unlikely. This leaves collisional excitation induced by shocks the most important mechanism to focus our attention and analysis on.

Before we consider shocks, we should emphasise that it is possible that AGN activity within our sample could produce an artificial enhancement of the $H_2/7.7\mu$m PAH ratio since weak AGNs are capable of influencing the chemistry and composition of nuclear regions within galaxies. The spectra of the inner few square kiloparsecs of 59 nearby galaxies (Smith et al. 2007b) suggest that the radiation from AGN may modify the grain

distribution, exciting unusual PAH emission. However, both AGN and dynamical shocks (Micelotta et al. 2010) can have impact close to the emitting source, destroying PAHs and rendering the H_2 to PAH ratio unreliable.

Since we have extracted large areas (see Table A5) that nominally include the nuclear region, but are not limited to it, the effect of AGN radiation that may be present will be lessened compared to the study of Smith et al. (2007b) which focused specifically on the nuclear region. Of the HCG MOHEGs with detected optical nuclear activity, we have one Seyfert galaxy (HCG 56B, Sy2), four optically classified as AGN (HCG 44A, 57A and 95C; Table 3) and four with LINER classifications. For HCG 57A, however, an extraction in the disk, well away from the nucleus, clearly shows H_2-enhancement (Fig. 5b). We note that the sources of LINER emission in galaxies is still under debate (see e.g. Yan & Blanton 2012), but recent work by Rich et al. (2011) find widespread LINER-like emission due to shocks in late-stage mergers.

If the 7.7μm PAH is tracing star formation (and not being depleted) in the HCG MOHEGS, we would expect it to scale approximately with the 24μm continuum emission (unless there is a strong contribution from AGN). Indeed, we show in Fig. 11b that elevated H_2/7.7μm PAH ratio's map to elevated H_2/24μm emission, except in the case of HCG 56B where the MOHEG emission may be due to excitation within an XDR or kinetic energy from a jet in this Seyfert galaxy. Based on its L_{H_2}/L_X ratio (see section D.2 of the Appendix) we can rule out XDR-heating and, in combination with its radio luminosity (Table D2), dissipation of kinetic energy provided by the AGN jet appears a more likely excitation mechanism.

The evidence presented here is most consistent with shock-excitation through dynamical interaction; nevertheless our current data does not allow us to definitively distinguish between shock excitation of H_2 (via H I cloud collisions or gas infall) or PAH depletion due to AGN, although the latter appears unlikely for the majority of cases based on their optical activity (Table 3).

5.2. *Collisional Excitation by Interaction of Galaxies with the Group IGM*

In the previous section we ruled out X-ray heating from within MOHEG galaxies as a mechanism for producing the observed enhanced H_2 emission. However, could interactions with the group IGM produce shock-heating of molecular hydrogen? Possible processes are ram pressure stripping due to a hot IGM, collisions with previously stripped tidal material (i.e. cold IGM), and finally material being accreted onto galaxies from the IGM.

Rasmussen et al. (2008) investigated the X-ray properties of H I-deficient groups and found the effect of ram pressure stripping to be small, only capable of removing small amounts of cold gas from group members. Unlike clusters, the relatively shallow gravitational potential well does not produce similarly high temperatures and luminosities of X-ray emission (see section D). Given the relative inefficiency of stripping by hot plasma, Rasmussen et al. (2008) find turbulent viscous stripping due to hydrodynamical interactions (e.g. Nulsen 1982) to be a more viable mechanism for removing gas in the HCG galaxies. The efficiency of viscous stripping may even be underestimated given that such processes may not be well treated by SPH (Smoothed Particle Hydrodynamics) schemes (Kawata & Mulchaey 2008). Therefore, of the H I-stripping mechanisms in compact groups, tidal interactions appear to dominate, but with viscous stripping potentially contributing significantly and ram-pressure stripping being at most a small effect(Rasmussen et al. 2008). Since tidal stripping could help to produce the material required for viscous stripping, we need to look for evidence of this material within the IGM of MOHEG groups.

Recent H I observations of HCGs have shown that even though the galaxies themselves are H I-deficient (Williams & Rood 1987; Verdes-Montenegro et al. 2001), a large diffuse-H I component exists in their IGM (Borthakur et al. 2010). We have also shown that for the MOHEG groups HCG 40 and HCG 91 (Figures 3 and 4, respectively), interferometric H I data hints at structure in between and around the galaxies. More recent VLA data (Verdes-Montenegro et al. in prep.) reveals more: the iso-velocity counters for HCG 40A appear to range from 6225 km s^{-1} to 6600 km s^{-1}, but are disturbed towards the location of HCG 40B (a MOHEG) located at $\sim$6800 km s^{-1}. H I in HCG 91 reveals streams connecting 91A and C, and further away B, as tentatively suggested by Figure 4.

Of the remaining MOHEG groups with recent VLA data (HCG 15, 25, 68 and 95) the majority, i.e. all except HCG 68, show evidence of interaction-driven disturbed H I (Verdes-Montenegro et al.; private communication). However, due to limitations of the interferometric data (sensitivity limits and resolving out emission), we cannot claim to have a complete picture of the H I distribution within the groups. Considering the groups individually, HCG 15A has no H I detected, however 15D (MOHEG) lies close to 15F spatially and at a similar recessional velocity (seen in the GBT data of Borthakur et al. 2010). The VLA data shows that HCG 15F (with no mid-infrared spectral coverage) has misaligned H I gas compared to its velocity field, indicative of a tidal stream. H I is detected around HCG 25B (MOHEG) and F, and forms a bridge-like structure to A. The MOHEG HCG 95C has associated H I, as well as adjacent gas corresponding to the optical velocity of 95A.

Given both the limitations of detecting more diffuse H I structures that (likely) exist in the groups, and that not all galaxies in each group were targeted by IRS (i.e. some MOHEG emission is likely missed due to the orientation of the slits), the presence of H I structures within MOHEG groups with available data could be indicative of a causal connection. As galaxies in compact groups travel through the clumpy IGM formed by numerous gravitational interactions, we could expect stochastic collisions between the inhomogeneous tidal H I and the disks of the galaxies where interactions of the gaseous components could lead to the formation of bow shocks (Nulsen 1982). High relative velocities and collisions with more dense H I concentrations in the IGM would produce stronger excited H_2 signatures. However, gas disks disrupted and heated due to the turbulent energy created in the collision would be more prone to viscous stripping (Nulsen 1982), due to hydrodynamic drag or hydro-instabilities, and would therefore lose gas in a similar way to traditional ram-pressure stripping by a hot medium. This may also play a role in transforming late-type disk galax-

ies into early-type disk systems (Quilis, Moore & Bower 2000).

If this is the case, the physical process producing the HCG H_2-enhanced galaxies is similar to what is observed in Stephan's Quintet, but with much lower relative velocities and therefore lower densities and lower ambient ISM pressure. This would limit the H I to H_2 conversion in the region experiencing the collision. Inspection of the groups included in this study show that groups with MOHEGs have velocity dispersions ranging from $\sim$100 km s^{-1} to 500 km s^{-1} (Hickson et al. 1992), whilst the broad H I profiles of the MOHEG HCGs (Borthakur et al. 2010) indicate that high-velocity dispersion ($\Delta V \sim 400-900$ km s^{-1}) cold gas is available in the IGM (with column densities $> 10^{19}$ cm^{-2}) in addition to tidal streams and clouds.

Lower kinetic energy in the interaction (from lower shock speeds) would not produce as luminous H_2 as seen in SQ. Nevertheless, the surface area of the leading disk edge and the distribution of broad H I clouds could produce significant warm H_2 mass emission and be detected by *Spitzer*. The limitations of slit coverage prevent us from making a definitive statement about the spatial distribution of shock-excited H_2, but the extraction areas (particularly that of LL which is sensitive to the strongest H_2 transitions) cover large parts of the disk, so even though we may have missed stronger emission towards the edges of galaxies, we are able to maximise obtaining a detection of excited H_2. Follow-up IRAM CO mapping (Lisenfeld et al, in prep.) in combination with optical AGN and shock diagnostics using VIRUS-P (Freeland et al, in prep.) and *Herschel* far-infrared spectral mapping will shed light on the mechanisms contributing to the observed evolution.

An alternative to a viscous stripping mechanism is accretion, where IGM tidal debris falls back onto group galaxies in streams that are low-to-medium velocity, thus fueling new star formation activity. If the gas is being decelerated abruptly, it would produce shock excitation, as well as additional fuel for star formation, shifting the galaxy from the red sequence to intermediate mid-infrared colours. Given the velocity dispersions in compact groups (Hickson et al. 1992) and complex gravitational interactions, it is not clear how common such events would be and how much gas could be added in this way.

The only HCG MOHEGs in this study that show significant star formation (based on their mid-infrared spectra) are 95C and 68C. HCG 95C has the intriguing combination of intermediate mid-infrared colours and a star forming spectrum that may indicate a recent increase in star formation relative to the galaxy's stellar mass. This may be due to tidal interactions or possibly a significant gas accretion event enhancing star formation (see Section 4.1.3). If a threshold of gas mass exists that must be accreted to generate excited H_2 , and an associated amount of star formation expected to be seen in these systems, detailed modelling is required to investigate this threshold. In the majority of HCG systems, however, no enhancement in star formation is found (Iglesias-Páramo & Vílchez 1998; Martínez et al. 2010) and instead evidence of truncation in early-type HCG galaxies (de la Rosa et al. 2007) and relatively low star formation rates (Bitsakis et al. 2011).

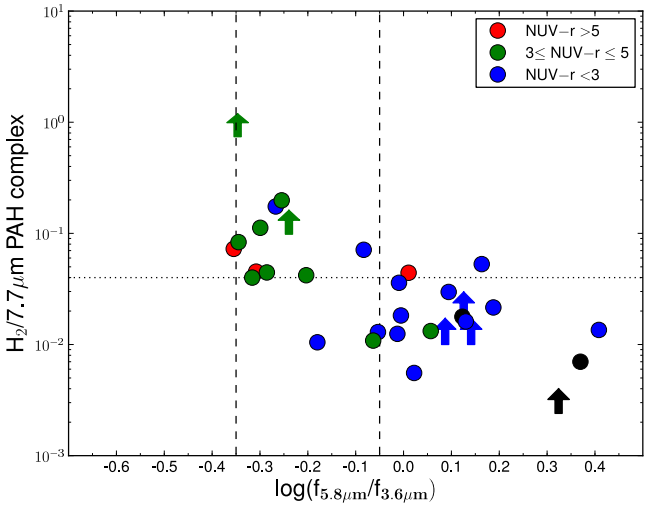

FIG. 14: $H_2/7.7\mu$m PAH ratio color-coded according to NUV-r color. The galaxies are divided into red sequence systems (red), blue cloud galaxies (blue) and green valley members (green) with black points representing galaxies with absent data. The vertical dashed lines indicate the mid-infrared green valley (from Equation 1).

6. THE MID-INFRARED "GREEN VALLEY": AN EVOLUTIONARY CONNECTION?

The observed underdensity of HCG galaxies at intermediate mid-infrared colors hints at active evolution from dusty star-forming to early type (as originally suggested by Johnson et al. 2007). The location of MOHEG galaxies (as shown in Figs 10 and 11), lying in the mid-infrared "green valley", provides a tantalising addition to the overall picture of transformation within HCGs.

Large area surveys have revealed an intermediate population in UV-optical color space: the "green valley" galaxies (Blanton et al. 2003). These are speculated to be undergoing active transformation from the"blue cloud" to the "red sequence". Given that Bitsakis et al. (2011) find over 50% of early-type and more than 60% of late-type galaxies in "dynamically old" groups are located in the optical green valley, there may exist a possible connection between HCG MOHEGS and the optical green valley.

Using the NUV and r-band photometry from Bitsakis et al. (2011), we determine extinction-corrected NUV−r colors for the HCG MOHEGs with available data. In Figure 14 we plot the $H_2/7.7\mu$m PAH values color-coded by NUV−r value, with 3 $\leq$NUV−r$\leq$ 5 in the optical green valley, NUV−r$>$ 5 belonging to the red sequence and NUV−r$<$ 3 designating the blue cloud. A large fraction of MOHEG galaxies lie either in the green valley or on the red sequence, with only three having blue NUV−r colors. The predominance of "green" NUV−r colors in the MOHEG sample is suggestive of a connection between H_2 enhancement and the star formation properties of the compact group systems.

Employing intermediate mid-infrared colors to define a mid-infrared "green valley" within compact groups has

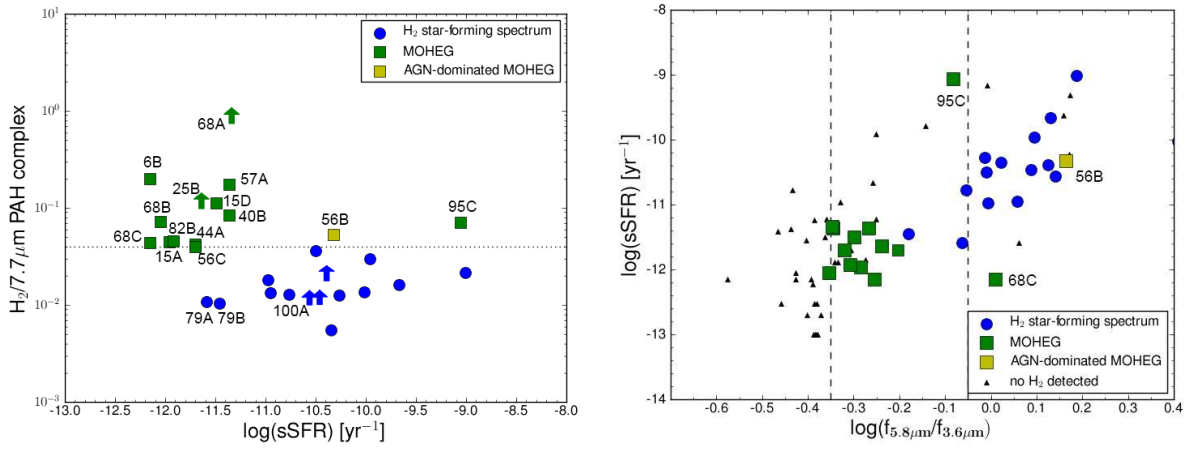

(a) (b)

FIG. 15: a) $H_2/7.7\mu$m PAH as a function of log sSFR (sSFR data from Bitsakis et al. 2011) with H_2 star-forming systems in blue, MOHEGs in green and AGN-dominated MOHEGs in yellow. b) Plotting log sSFR against $\log[f_{5.8\mu m}/f_{3.6\mu m}]$ shows that the majority of MOHEGs (in green) may form a transitional population between star-forming and early-type systems. AGN-dominated MOHEGs are shown in yellow, H_2-detected star-forming galaxies in blue and non-H_2 detections as black triangles.

the advantage of mitigating dust obscuration, which affects the NUV−r color heavily. In dense environments, where interactions cause gas and dust to be stripped from galaxies, this may be a key tracer of transformation (e.g. the Coma Infall region; Walker et al. 2012). Furthermore, utilising mid-infrared colors from *Spitzer* and *WISE*, particularly to select dusty, early-type galaxies, may help uncover the ubiquity of active transformation in a variety of environments.

To investigate this further, we look at the specific star formation rates (sSFR) of galaxies in our sample in common with that of Bitsakis et al. (2011). Their sSFR (SFR per unit old stellar mass) is based on SED (spectral energy distribution) fitting and 2μm near-infrared luminosity.

The majority of HCG MOHEGs occupy a narrow range in sSFR ($-12.3 < \log(\mathrm{sSFR})[\mathrm{Gyr}^{-1}] < -11.3$), except for the somewhat unusual HCG 95C (see section 4.1.3) and the AGN-dominated system HCG 56B (Fig. 15a). This suggests that the mechanism producing enhanced excited H_2 in these systems is somewhat different to the other MOHEGs. In the case of HCG 95C, a merger or gas accretion may explain the increased star formation in relation to stellar mass, producing shock-excited H_2 as a by-product. In HCG 56B, a jet interacting with the ISM is a possible source of excess excited H_2, which elevates it above the H_2 star-forming systems with similar sSFR.

Figure 15b plots our entire galaxy group sample with sSFR taken from Bitsakis et al. (2011). The $\log[f_{5.8\mu m}/f_{3.6\mu m}]$ color – sensitive to star formation through the continuum and 6.2μm PAH, divided by the 3.6μm emission tracing stellar mass– appears to act as a general proxy for sSFR. This is not surprising since the $\log[f_{5.8\mu m}/f_{3.6\mu m}]$ color tracks the $\log[f_{8.0\mu m}/f_{3.6\mu m}]$ color closely: the 8.0μm band is dominated by the 7.7μm PAH tracing star formation, normalized by the 3.6μm light that tracing stellar mass. The majority of HCG MOHEGs appear to lie at low-intermediate sSFR i.e. at the red end of the early-type population. This suggests that the HCG MOHEGs may be a transitional population between the two main populations, and that the warm H_2 emission is connected to the mechanism driving the bimodality in mid-infrared color, actively moving systems onto the optical red sequence.

A notable exception to this picture, HCG 68C, lies well below the actively star-forming cloud in disagreement with its mid-infrared color. A possible explanation is that its star formation rate has been underestimated ($0.05\,M_\odot yr^{-1}$; Bitsakis et al. 2011) since Martínez-Badenes (2012) find a SFR of $1.46\,M_\odot yr^{-1}$ and log(sSFR) of -10.70 yr^{-1}, which would move it to the blue cloud of actively star-forming galaxies.

6.1. *Comparison with other samples*

Ogle et al. (2010) have shown that jet-ISM interactions can efficiently produce excited H_2 in radio-loud galaxies. Since we have ruled out this mechanism in the majority of HCG MOHEGs, we now consider whether the phenomenon of enhancement in warm H_2 emission could be linked to the environment of the host. For example, several nearby dusty early type galaxies reveal strong H_2 emission associated with almost negligible star formation (Kaneda et al. 2008; Vega et al. 2010). Recent accretion events have been suggested as a mechanism, particularly since some systems show star/gas counter-rotating disks. The shocks believed to give rise to the observed warm H_2 emission could arise from a mechanism such as gas infall or a minor merger delivering additional gas, that then fuels a rejuvenation event (Vega et al. 2010). The ellipticals in Kaneda et al. (2008) were chosen to be X-ray-bright, dusty systems, with some having known jets (making jet-ISM interactions a possible mechanism) and other containing LLAGN.

A connection between H_2-enhanced systems and LINER-like optical emission is not clear. All four of the early types in the sample of Vega et al. (2010) are classified as LINERs, and, within the SINGS sample, galaxies classified as LINERs as well as Seyfert galaxies show en-

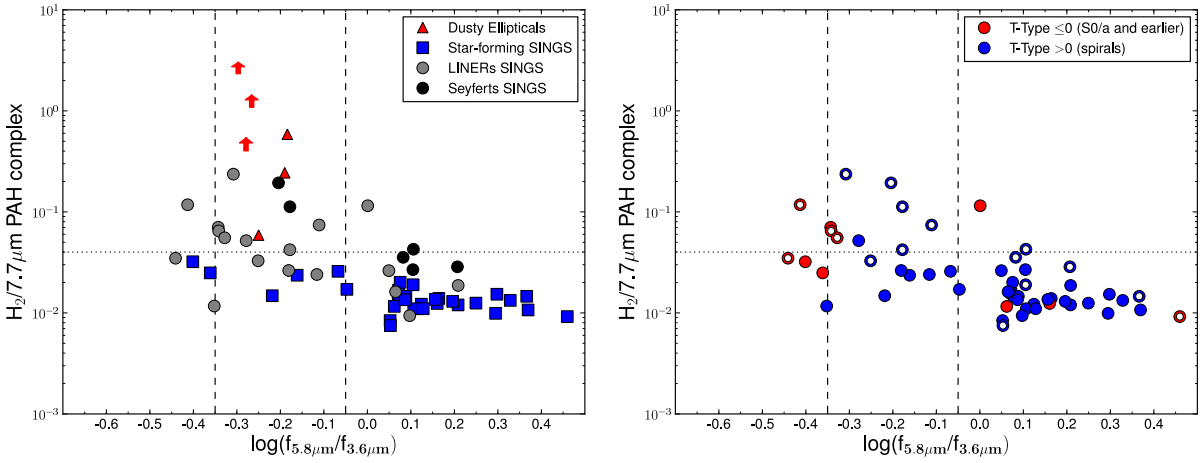

FIG. 16: a) The Kaneda et al. (2008) dusty ellipticals (red) and SINGS H_2-detected galaxies are plotted as a function of $\log[f_{5.8\mu m}/f_{3.6\mu m}]$ color, where the vertical dashed lines indicate the mid-infrared green valley (from Equation 1). SINGS star-forming systems are shown in blue (squares), LINER systems are grey (circles) and Seyferts are in black (circles). b) The SINGS sample is plotted in terms of T-type (late-type in blue, early type in red), with open circles indicating galaxies in dense/interacting environments.

hanced excited H_2 emission (Roussel et al. 2007; Ogle et al. 2010).

In Figure 16a we plot six of the Kaneda et al. (2008) systems (with archival IRAC photometry) and the SINGS sample (Roussel et al. 2007; Dale et al. 2005), as a function of $\log[f_{5.8\mu m}/f_{3.6\mu m}]$ color. We see that the dusty ellipticals from Kaneda et al. (2008) and several SINGS LINERs occupy a similar phase space compared to the HCG MOHEGs. However, the SINGS sample was not chosen to be uniform, but instead representative of nearby galaxies; several systems are located in dense environments such as clusters. In Figure 16b we show the SINGS galaxies as a function of T-type and plot galaxies that are located in a dense or interacting environment (Virgo, Fornax, Dorado clusters, compact group, pair or triple) as an open circle. We notice more spiral systems inhabit the red end of the mid-infrared green valley, compared to HCGs where this region is dominated by S0/a types. Intriguingly, this distribution appears somewhat similar to the HCG distribution in $H_2/7.7\mu$m PAH space. However, we cannot rule out AGN being the source of excitation in the Kaneda et al. (2008) and SINGS MOHEG systems.

The effect of environment on the evolution of a galaxy is still contentiously debated. Compact groups are relatively rare, but given their strong gravitational interactions, and relatively shallow potential-wells, may provide an opportunity to understand related mechanisms at work in high-density clusters, as well as loose groups. For example, comparisons with several different control samples led Walker et al. (2010, 2012) to conclude that the observed IRAC color bimodality in their sample of HCGs was a direct consequence of environment and appeared most similar to the distribution found for the Coma infall region.

7. DISCUSSION

Recent studies have explored the connection between dense environments and the formation of early-type disk and lenticular galaxies. HCGs may be the ideal laboratory to study how galaxies are being "pre-processed" and transformed by mechanisms within groups and clusters.

The simulations of Bekki & Couch (2011) indicate that the compact group environment, causing gas stripping and bulge building via tidal interactions, preferentially form S0's from spirals. They predict long tidal streams, broken rings and seemingly isolated massive clouds of neutral gas within the IGM. Deep H I observations are uncovering these kind of features (e.g. in HCG 44, Serra et al. 2012b), as well as the strong dependence of the H I morphology of early-type galaxies on environment (Serra et al. 2012a). The pre-processing mechanisms occurring in groups may be key to explaining the morphology-density relation as observed in field and cluster galaxies (Postman & Geller 1984).

Observationally, Bitsakis et al. (2011) find that S0's dominate dynamically evolved HCGs and are preferentially found in the optical green valle. If we believe that these systems are not passively evolving, but instead show accelerated evolution from the blue cloud to the red sequence, there may be a connection to the MOHEGs observed in the mid-infrared green valley.

We have discussed the possibility that interactions with tidal debris may be a valid mechanism within compact groups, and would therefore show evidence of extended shock emission. Although we have some indication that in many cases the observed warm H_2 is extended on scales larger than the LL slit, without maps we lack crucial spatial information. Detailed shock diagnostic observations are currently underway with both optical IFU (Integral Field Unit) measurements and resolved *Herschel* spectroscopy of far-infrared cooling lines, such as high-J CO, H_2O, [C II] and [O I].

Tidal interactions combined with viscous stripping could produce accelerated evolution from late-type to

early-type and may help explain systems with evidence of H I-deficiency and truncated H I disks that cannot be explained by simple ram pressure arguments. For example, in the Pegasus I cluster (Levy et al. 2007) the same correlation between sSFR and H I-deficiency is observed in this lower density, low velocity dispersion system as found in Virgo (Rose et al. 2010). They find that sSFR within H I-depleted disks is lower, but that the sSFR of the nucleus relative to the global value increases with H I deficiency. This suggests a mechanism that builds stellar mass in the bulge, but decreases H I and star formation in the disk. The evidence for suppression of star formation in low-redshift galaxy groups found by Rasmussen et al. (2012) may be related to such a mechanism. In this study *GALEX* imaging indicates that, on average, the sSFR of star-forming galaxies in groups is suppressed by ∼40% relative to the field.

8. CONCLUSIONS

In this paper we have presented the results of a mid-infrared spectral and photometric study of 74 galaxies in 23 Hickson Compact Groups using the *Spitzer Space Telescope* with the goal of searching for enhanced H_2 emission and its possible connection to evolution within HCGs. We highlight here our primary conclusions:

- Searching for excited H_2 in the intragroup medium have led to two tentative detections, located at the edges of two disk galaxies in HCG 40 and 91, respectively. Large-scale intragroup warm H_2 emission as seen in Stephans' Quintet, appears to be rare.
- We have detected warm H_2 in 32 galaxies with 14 MOHEG (Molecular Hydrogen Emission Galaxies) systems, i.e. H_2 emission in excess of what is expected from UV excitation associated with star formation. The observed $H_2/7.7\mu$m PAH ratios may be due to either shock-induced excitation of H_2 or, in a small minority of systems, possible PAH depletion due to AGN activity.
- The luminosity of X-rays detected in MOHEG galaxies with archival data is insufficient to heat the observed amounts of excited H_2. We find that in the majority of systems, AGN activity is unlikely to be responsible for the observed H_2-enhancement. This leaves the possibility of shock-excitation through interaction with the IGM as a plausible mechanism for producing the observed emission.
- The presence of copious intragroup H I suggests that collisional excitation may be due to galaxies passing through this debris, thus experiencing shock heating of their disks – analogous, but less energetic to what is seen in the SQ shock. The heated gas disks undergoing viscous stripping may accelerate evolution from the blue cloud across the green valley. The previously stripped material may also accrete back onto the galaxies, shock-heating the disk gas and providing fuel for "new" star formation.
- The MOHEG systems are mainly early-type disks and lie chiefly within a mid-infrared "green valley" between the population of dusty star formers and early type galaxies. The optical colours of the majority of these systems lie in the NUV−r "green valley", and their locus in specific star formation suggests they may form a transitional population moving onto the red sequence.
- Interactions within a group, pair or triple environment may be producing similar H_2-enhancement accompanied by non-passive evolution in mid-infrared or optical colour, as seen in the SINGS sample.

We thank the referee for helpful comments and suggestions that improved the content and clarity of this paper. We are grateful to Sanch Borthakur (Johns Hopkins University) for access to unpublished H I data and Michael Brown (Monash University) for the use of his galaxy template library. This work is based on observations made with the *Spitzer* Space Telescope, which is operated by the Jet Propulsion Laboratory, California Institute of Technology under NASA contract 1407. MEC acknowledges support from the Australian Research Council (FS110200023). Support for this work was provided by NASA through an award issued by JPL/Caltech. UL acknowledges support by the research projects AYA2007-67625-C02-02 and AYA2011-24728 from the Spanish Ministerio de Ciencia y Educaci ón and the Junta de Andaluc ía (Spain) grant FQM108. LVM is funded by Grant AYA2008-06181-C02 and AYA2011-30491-C02-01, co-financed by MICINN and FEDER funds, and the Junta de Andaluca (Spain) grants P08-FQM-4205 and TIC-114. This research has made use of the NASA/IPAC Extragalactic Database (NED) which is operated by the Jet Propulsion Laboratory, California Institute of Technology, under contract with the National Aeronautics and Space Administration. This research has made use of data obtained from the Chandra Source Catalog, provided by the Chandra X-ray Center (CXC) as part of the Chandra Data Archive.

REFERENCES

Allen, M.G., Groves, B.A., Dopita, M.A., Sutherland, R.S., & Kewley, L.J. 2008, ApJ, 178, 20
Allen, R.J., & Sullivan, W.T., III. 1980, A&A, 84, 181
Amram, P., Plana, H., Mendes de Oliveira, C., Balkowski, C., & Boulesteix, J. 2003, A&A, 402, 865
Appleton, P.N. et al. 2006, ApJ, **639**, L51
Barnes, D. G., & Webster, R. L. 2001, MNRAS, 324, 859
Bekki, K., & Couch, W. J. 2011, MNRAS, 415, 1783
Bernard-Salas, J., Spoon, H. W. W., Charmandaris, V., et al. 2009, ApJS, 184, 230
Bitsakis, T., Charmandaris, V., da Cunha, E., et al. 2011, A&A, 533, A142
Blanton, M. R., Hogg, D. W., Bahcall, N. A., et al. 2003, ApJ, 594, 186
Borthakur, S., Yun, M., & Verdes-Montenegro, L. 2010, ApJ, 710, 385
Brinchmann, J., Charlot, S., Heckman, T. M., et al. 2004, arXiv:astro-ph/0406220
Cluver, M. E., Appleton, P. N., Boulanger, F., et al. 2010, ApJ, 710, 248
Condon, J. et al. 1998, AJ, 115, 1693
Cortese, L., Gavazzi, G., Boselli, A., Franzetti, P., Kennicutt, R. C., O'Neil, K., & Sakai, S. 2006, A&A, 453, 847

Coziol, R., Andernach, H., Caretta, C. A., Alamo-Martínez, K. A., & Tago, E. 2009, AJ, 137, 4795
Coziol, R., & Plauchu-Frayn, I. 2007, AJ, 133, 2630
Coziol, R., Brinks, E., & Bravo-Alfaro, H. 2004, AJ, 128, 68
da Cunha, E., Charlot, S., & Elbaz, D. 2008, MNRAS, 388, 1595
Dale, D. A., Cohen, S. A., Johnson, L. C., et al. 2009, ApJ, 703, 517
Dale, D. A., Smith, J. D. T., Armus, L., et al. 2006, ApJ, 646, 161
Dale, D. A., Bendo, G. J., Engelbracht, C. W., et al. 2005, ApJ, 633, 857
Dalgarno, A., Yan, M., & Liu, W. 1999, ApJS, 125, 237
Da Rocha, C., Ziegler, B. L., & Mendes de Oliveira, C. 2008, MNRAS, 388, 1433
de la Rosa, I. G., de Carvalho, R. R., Vazdekis, A., & Barbuy, B. 2007, AJ, 133, 330
Desai, V., Armus, L., Spoon, H. W. W., et al. 2007, ApJ, 669, 810
Desjardins, T. D., Gallagher, S. C., Tzanavaris, P., et al. 2012, arXiv:1212.1151
de Vaucouleurs, G., de Vaucouleurs, A., Corwin, H. G., Jr., Buta, R. J., Paturel, G., & Fouque, P. 1991, Volume 1-3, XII, 2069 pp. 7 figs.. Springer-Verlag Berlin Heidelberg New York
de Vaucouleurs, G., de Vaucouleurs, A., Corwin, H. G., Jr., et al. 1992, VizieR Online Data Catalog, 7137, 0
Dopita, M. A., & Sutherland, R. S. 1996, ApJS, 102, 161
Draine, B. T., & Woods, D. T. 1992, ApJ, 387, 732
Dressler, A. 1980, ApJ, 236, 351
Durbala, A., del Olmo, A., Yun, M. S., et al. 2008, AJ, 135, 130
Evans, I. N., Primini, F. A., Glotfelty, K. J., et al. 2010, ApJS, 189, 37
Fazio, G. G., Hora, J. L., Allen, L. E., et al. 2004, ApJS, 154, 10
Forbes, D. A. et al. 2006, PASA, 23, 38
Gallagher, S. C., Durrell, P. R., Elmegreen, D. M., et al. 2010, AJ, 139, 545
Gao, Y., & Xu, C. 2000, ApJ, 542, L83
Governato, F., Tozzi, P., & Cavaliere, A. 1996, ApJ, 458, 18
Guillard, P., Boulanger, F., Pineau Des Forêts, G., & Appleton, P. N. 2009, A&A, 502, 515
Guillard, P., Boulanger, F., Pineau des Forêts, G., et al. 2012, ApJ, 749, 158
Guillard, P., Ogle, P. M., Emonts, B. H. C., et al. 2012, ApJ, 747, 95
P., Busarello, G., et al. 2011, MNRAS, 417, 2831
Helou, G., Roussel, H., Appleton, P., et al. 2004, ApJS, 154, 253
Hickson, P. 1982, ApJ, 255, 382
Hickson, P., Kindl, E., & Auman, J. R. 1989, ApJS, 70, 687
Hickson, P., Mendes de Oliveira, C., Huchra, J. P., & Palumbo, G. G. 1992, ApJ, 399, 353
Ho, L. C. 2008, ARA&A, 46, 475
Hollenbach, D. J., & Tielens, A. G. G. M. 1997, ARA&A, 35, 179
Houck, J. R., Roellig, T. L., Van Cleve, J., et al. 2004, Proc. SPIE, 5487, 62
Huchtmeier, W. K. 1997, A&A, 325, 473
Iglesias-Páramo, J., & Vílchez, J. M. 1998, AJ, 518, 94
Iglesias-Páramo, J., & Vílchez, J. M. 1998, AJ, 115, 1791
Johnson, K.E., Hibbard, J.E., Gallagher, S.C., Charlton, J.C., Hornschemeier, A.E., Jarrett, T.H.& Reines, A.E. 2007, AJ, 134, 1522
Kaneda, H., Onaka, T., Sakon, I., Kitayama, T., Okada, Y., & Suzuki, T. 2008, ApJ, 684, 270
Kawata, D., & Mulchaey, J. S. 2008, ApJ, 672, L103
Khachikian, E. Y., & Weedman, D. W. 1974, ApJ, 192, 581
Lacy, M., Storrie-Lombardi, L. J., Sajina, A., et al. 2004, ApJS, 154, 166
Leon, S., Combes, F., & Menon, T. K. 1998, A&A, 330, 37
Lepp, S., & McCray, R. 1983, ApJ, 269, 560
Levy, L., Rose, J. A., van Gorkom, J. H., & Chaboyer, B. 2007, AJ, 133, 1104
Maloney, P. R., Hollenbach, D. J., & Tielens, A. G. G. M. 1996, ApJ, 466, 561
Martínez, M. A., Del Olmo, A., Coziol, R., & Perea, J. 2010, AJ, 139, 1199
Martínez-Badenes, V., Lisenfeld, U., Espada, D., et al. 2012, A&A, 540, A96
Mendes de Oliveira, C., & Hickson, P. 1994, ApJ, 427, 684
Micelotta, E. R., Jones, A. P., & Tielens, A. G. G. M. 2010, A&A, 510, A36
Mulchaey, J. S., Davis, D. S., Mushotzky, R. F., & Burstein, D. 2003, ApJS, 145, 39
Neufeld, D. A., Hollenbach, D. J., Kaufman, M. J., et al. 2007, ApJ, 664, 890
Nulsen, P.E.J. 1982, MNRAS, 198, 1007
Ogle, P., Antonucci, R., Appleton, P., & Whysong, D. 2007, ApJ, 668, 699
Ogle, P., Boulanger, F., Guillard, P., Evans, D.A., Antonucci, R., Appleton, P.N, Nesvadba, N. & Leipski, C. 2010, ApJ, 724, 1193
Osmond, J. P. F., & Ponman, T. J. 2004, MNRAS, 350, 1511
Osterbrock, D. E., & Martel, A. 1993, ApJ, 414, 552
Peterson, B., Appleton, P., Helou, G., Jarrett, T., Cluver, M., Ogle, P., Guillard, P., Struck, C., Boulanger, F., 2011, ApJ, 751, 11
Ponman, T. J., Bourner, P. D. J., Ebeling, H., Böhringer, H. 1996, MNRAS, 283, 690
Postman, M., & Geller, M. J. 1984, ApJ, 281, 95
Quilis, V., Moore, B. & Bower 2000, Science, 288, 1617
Radovich, M., Rafanelli, P., & Barbon, R. 1998, A&A, 334, 124
Rasmussen, J., Ponman, T. J., Verdes-Montenegro, L., Yun, M. S., & Borthakur, S. 2008, MNRAS, 388, 1245
Rasmussen, J., Mulchaey, J.S., et al. 2012, arXiv:1208.1762
Rieke, G. et al., 2004, ApJS, 154, 204
Rich, J. A., Kewley, L. J., & Dopita, M. A. 2011, ApJ, 734, 87
Rose, J. A., Robertson, P., Miner, J., & Levy, L. 2010, AJ, 139, 765
Roussel, H., et al. 2007, ApJ, 669, 959
Rubin, V.C., Hunter, D.A., & Ford, W.K.J. 1991, ApJS, 76, 153
Sanders, D. B., Mazzarella, J. M., Kim, D.-C., Surace, J. A., & Soifer, B. T. 2003, AJ, 126, 1607
Serra, P., Oosterloo, T., Morganti, R., et al. 2012, MNRAS, 422, 1835
Serra, P. et al. 2012, arXiv:1209.4107
Shapiro, K. L.,
Shull, J. M., & Hollenbach, D. J. 1978, ApJ, 220, 525
Smith, J.D.T. et al. 2009, ApJ, 693, 713
Smith, J. D. T., Armus, L., Dale, D. A., et al. 2007, PASP, 119, 1133
Smith, J. D. T., Draine, B. T., Dale, D. A., et al. 2007, ApJ, 656, 770
Tang et al. 2011
Trinchieri, G., Sulentic, J., Pietsch, W., & Breitschwerdt, D. 2005, A&A, 444, 697
Tzanavaris, P., Hornschemeier, A. E., Gallagher, S. C., et al. 2010, ApJ, 716, 556
Vega, O. et al. 2010, ApJ, 721, 1090
Verdes-Montenegro, L., Yun, M. S., Williams, B. A., Huchtmeier, W. K., Del Olmo, A., & Perea, J. 2000, IAU Colloq. 174, Small Galaxy Groups, ed. M. Valtonen & C. Flynn (San Francisco: ASP), 167.
Verdes-Montenegro, L., Yun, M.S., Williams, B.A., Huchtmeier, W.K., Del Olmo, A., & Perea, J. 2001, A&A, 377, 812
Verdes-Montenegro, L., Yun, M. S., Perea, J., del Olmo, A., & Ho, P. T. P. 1998, ApJ, 497, 89
Walker, L. M., Johnson, K. E., Gallagher, S. C., et al. 2012, AJ, 143, 69
Walker, L. M., Johnson, K. E., Gallagher, S. C., Hibbard, J. E., Hornschemeier, A. E., Tzanavaris, P., Charlton, J. C., & Jarrett, T. H. 2010, AJ, 140, 1254
Westmeier, T., Braun, R., & Koribalski, B. S. 2011, MNRAS, 410, 2217
Williams, B. A., & Rood, H. J. 1987, ApJS, 63, 265
Yan, R., & Blanton, M. R. 2012, ApJ, 747, 61
Yun, M. S., Verdes-Montenegro, L., del Olmo, A., & Perea, J. 1997, ApJ, 475, L21

APPENDIX

A. THE HCG SAMPLE AND ASSOCIATED DATA

In this section we list all the galaxies that formed part of the parent HCG galaxy sample and the IRAC photometry measurements of each (as outlined in Section 3.2). Table A1 provides the photometry for each galaxy in the sample and if a warm H_2 detection was made.

TABLE A1: Measured IRAC Fluxes of HCG Sample

Galaxy	H_2-detected	3.6μm (mJy)	4.5μm (mJy)	5.8μm (mJy)	8.0μm (mJy)
6A	no	6.71	4.28	2.70	1.63
6B	yes	7.78	5.12	4.10	4.93
6C	no	5.81	3.72	2.37	1.64
6D	no	0.95	0.68	0.50	0.68
8A	no	11.37	7.42	4.65	3.04
8C	no	5.99	3.86	2.73	2.14
8D	no	5.72	3.72	2.45	2.25
15A	yes	18.32	11.63	9.49	11.59
15C	no	13.79	8.72	5.87	3.53
15D	yes	8.13	5.49	4.08	3.01
25B	yes	18.33	12.09	10.56	12.10
25D	no	3.72	2.44	1.53	1.22
25F	no	2.86	1.82	1.25	0.79
31A+C	yes	13.54	10.37	28.55	73.86
31B	no	2.46	1.69	2.23	4.42
40A	no	35.53	22.12	16.21	11.22
40B	yes	10.11	6.41	4.57	3.50
40C	yes	23.77	16.22	29.04	73.88
40D	yes	16.61	11.15	18.93	61.31
44A	yes	292.17	185.70	182.89	309.77
44B	no	–	96.29	–	38.56
44D	yes	13.46	9.11	20.74	49.71
47A†	yes	20.71	13.31	20.26	52.28
47B†	no	11.84	7.23	4.05	2.41
47D†	no	3.59	2.37	2.33	6.37
54A	no	1.14	0.78	0.82	1.39
54B†	no	3.70	2.90	5.50	11.10
54C†	no	1.25	0.80	1.80	4.10
55A†	no	6.53	3.93	2.66	1.22
55B†	no	3.44	2.15	1.33	0.72
55C†	yes	5.51	3.80	3.91	10.91
55D†	no	6.76	4.36	6.10	12.97
56B	yes	$^\diamond$25.36	$^\diamond$30.84	36.94	52.30
56C	yes	5.82	3.71	2.81	2.45
56D	yes	4.08	2.90	5.45	14.53
56E	yes	2.12	1.43	2.06	4.08
57A	yes	31.11	20.04	16.82	20.15
57B	no	14.36	9.14	8.04	12.47
57C	no	10.88	6.99	4.51	2.64
57D	no	7.83	5.26	8.40	19.69
57E	no	8.98	5.77	4.43	5.23
62A	no	94.42	58.58	38.77	54.16
62B	no	15.16	9.36	6.27	4.26
62C	no	14.69	9.46	5.93	3.24
67A†	no	54.40	34.10	20.40	16.10
67B†	yes	30.70	20.80	32.30	72.30
67D†	no	5.30	3.30	2.30	1.80
68A	yes	226.63	136.56	101.99	61.77
68B	yes	108.76	66.57	48.04	33.19
68C	yes	111.70	69.21	114.44	248.81
75A†	no	13.10	10.40	5.70	5.10
75C†	no	4.00	2.40	1.60	1.30
75D†	yes	3.30	2.10	3.40	11.80
75E	no	3.70	2.37	1.51	0.93
79A	yes	16.09	10.58	13.91	26.10
79B	yes	14.53	9.15	9.60	15.00
79C†	no	10.22	5.71	4.03	2.04
82A	no	15.69	10.06	6.56	3.94
82B	yes	12.78	8.02	5.98	6.96
82C	yes	8.54	6.24	15.12	47.75
91A	yes	*74.57	$^\diamond$59.87	92.65	608.84
91C	yes	8.68	5.88	11.71	30.63
91D	no	10.97	7.21	5.15	4.35
95A†	no	18.00	11.01	6.70	7.82
95C†	yes	7.05	4.27	4.89	10.60

Galaxy	H_2-detected	3.6μm (mJy)	4.5μm (mJy)	5.8μm (mJy)	8.0μm (mJy)
96A[a]	yes	80.15	107.86	187.72	328.56
96B	no	17.71	12.09	8.69	5.46
96C[b]	yes	8.86	6.21	11.76	29.78
97A[†]	no	19.90	12.70	7.90	6.0
97C[†]	no	13.20	7.80	3.50	2.20
97D[†]	no	15.50	9.30	5.80	4.10
100A	yes	40.38	25.93	35.70	156.89
100B	no	5.49	3.95	8.15	18.58
100C	no	3.65	2.56	3.58	7.14

[a] Measured using short exposure (1.2s) HDR image
[b] Contamination from 96A
[◇] Flux may be underestimated by ∼5% due to peak pixel non-linearity
[⋆] Flux may be underestimated by ∼10% due to peak pixel non-linearity
[†] Photometry from Bitsakis et al. (2011)

For systems with detected excited H_2 emission lines, the measured fluxes are presented in Table A2. Several systems have their SL and LL lines presented separately due to the regions sampled by the IRS not overlapping (and therefore not joined together). In addition, spectra that are not centered on the nucleus (therefore dominated by emission from the disk) are indicated. The strengths of the PAH complexes and atomic emission lines for the H_2-detected systems are presented in Tables A3 and A4. For galaxies without SL coverage, the IRAC inferred 7.7μm PAH values are: 8.77×10^{-15} W.m^{-2}, 1.33×10^{-14} W.m^{-2} and 1.68×10^{-15} W.m^{-2} for 40C, 44A and 75D, respectively.

The extracted areas of the H_2-detected galaxies are listed in Table A5, as well as any scaling factors employed to match the LL and SL spectral orders. The scaling between modules makes the assumption that the emission lines scale with the continuum i.e. the SL spectrum is scaled to bring it in line with the LL spectrum continuum. As an independent check we use the 7.7μm PAH and 11.3μm PAH emission features compared to the matched 24μm photometry. For systems not dominated by AGN heating, these measures should scale similarly with star formation. We plot these comparisons in Figure A1 for systems where the respective PAH emission lines are well-determined and the spectra (and global mid-infrared colors) are not AGN-dominated. Since systems that have been scaled show the same behaviour as those that have not, the scaling does not appear to have produced inconsistent fluxes. Uncertainties in the SL scaling factor (due to noise of the continuum) are estimated to be <0.02, corresponding to a flux uncertainty of <5%.

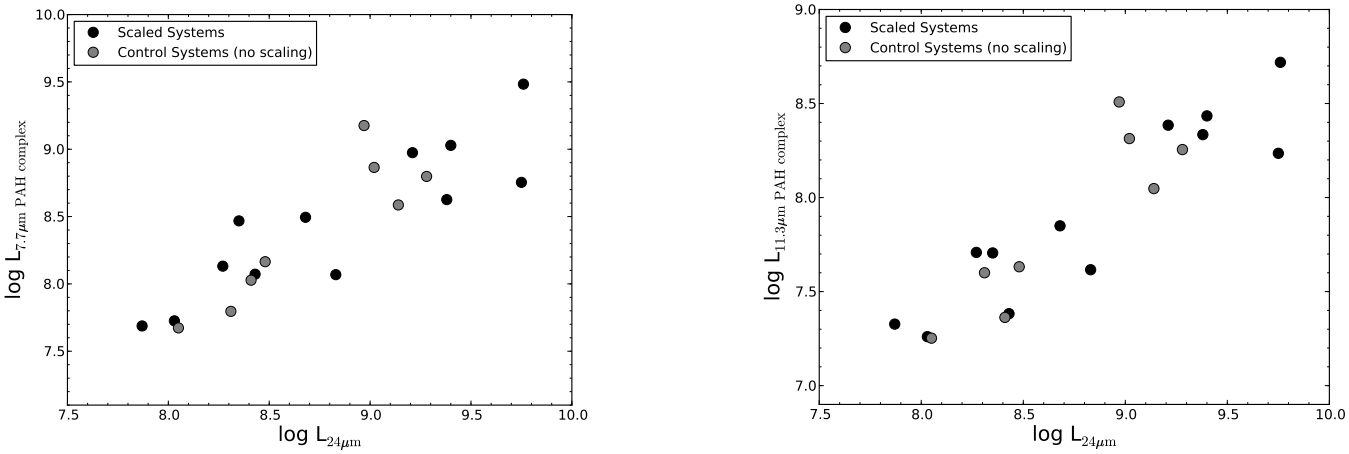

(a) Comparison of 7.7μm PAH and 24μm Luminosity

(b) Comparison of 11.3μm PAH and 24μm Luminosity

FIG. A1: Comparison of scaled and unscaled continuum and emission features

B. SPECTRA OF NON-MOHEG H_2 DETECTIONS

The spectra of the non-MOHEG H_2-detected HCG galaxies are shown in Figure B1 and B2. As expected, the majority of spectra appear consistent with star-forming systems, having excited H_2 associated with PDRs and UV excitation. The spectrum of HCG 96A indicates the presence of a powerful AGN given the prominent hot and warm dust and strong high excitation lines (Fig. B2f), also reflected in its mid-infrared colors. This galaxy is a known LIRG (Sanders et al. 2003) and Seyfert 2 galaxy (Osterbrock & Martel 1993).

TABLE A2: Observed H_2 Fluxes in units of $W\,m^{-2}$

Source	H_2 0-0 S(0) λ28.21μm	H_2 0-0 S(1) λ17.03μm	H_2 0-0 S(2) λ12.28μm	H_2 0-0 S(3) λ9.66μm	H_2 0-0 S(4) λ8.03μm	H_2 0-0 S(5) λ6.91μm
6B	1.710e-18 (5.093e-19)	8.440e-18 (8.113e-19)	1.251e-18 (5.748e-19)$^{\square}$	6.185e-18 (1.739e-18)	<3.751e-18	<3.151e-18†
15A	<2.605e-18	4.796e-18 (8.951e-19)	<2.446e-18	3.216e-18 (1.186e-18)	<5.385e-18	6.149e-18 (1.819e-18)
15D	2.920e-18 (1.019e-18)	1.107e-17 (1.864e-18)	3.750e-18 (1.719e-18)$^{\square}$	8.811e-18 (2.345e-18)	<2.367e-17	<6.414e-18 †
25B*	–	–	7.643e-19 (4.799e-20)	2.535e-18 (1.202e-19)	<8.727e-19	2.012e-18 (2.728e-19)†
25B$^{\diamond\bullet}$	<1.853e-18	1.159e-17 (1.979e-19)	–	–	–	–
31A+C$^{\star\bullet}$	–	–	1.731e-19 (3.424e-20)$^{\square}$	1.329e-19 (5.397e-20)$^{\square}$	<3.332e-19	< 7.815e-19
31A+C$^{\diamond}$	<1.423e-17	2.004e-17 (3.924e-20)	–	–	–	–
40B	<2.673e-18	5.619e-18 (1.081e-18)	<9.519e-19	3.457e-18 (1.063e-18)$^{\square}$	4.550e-18 (1.920e-18)$^{\square}$	<1.631e-18†
40C$^{\star\bullet}$	–	–	<1.966e-19	3.932e-19 (1.611e-19)$^{\square}$	<6.603e-19	4.335e-19 (2.012e-19)$^{\square\dagger}$
40C$^{\diamond}$	1.857e-17 (1.602e-18)	7.308e-17 (1.093e-19)	–	–	–	–
40D	9.173e-18 (3.047e-18)$^{\square}$	2.697e-17 (2.675e-18)	1.084e-17 (1.256e-18)$^{\square}$	2.009e-17 (1.693e-18)	<8.889e-18	6.978e-18 (2.348e-18)$^{\square}$
44A$^{\star\bullet}$	–	–	2.124e-18 (2.083e-19)$^{\square}$	3.245e-18 (2.542e-19)$^{\square}$	4.527e-18 (1.047e-18)$^{\square}$	7.281e-18 (9.326e-19)$^{\square\dagger}$
44A$^{\diamond}$	2.693e-17 (5.940e-18)	1.069e-16 (3.014e-20)	–	–	–	–
44D	9.598e-18 (3.674e-18)	5.243e-17 (8.442e-18)	<1.261e-17	<3.129e-16	<7.616e-17	3.302e-17 (1.337e-17)$^{\square\dagger}$
47A	<8.042e-18	2.556e-17 (3.100e-18)	7.745e-18 (3.100e-18)$^{\square}$	<1.769e-17	1.928e-17 (8.152e-18)$^{\square}$	<1.534e-17†
55C	1.056e-18 (1.718e-19)	3.927e-18 (3.630e-19)	1.445e-18 (3.084e-19)$^{\square}$	3.411e-18 (5.093e-19)	3.035e-18 (6.191e-19)$^{\square}$	<5.632e-18†
56B	<6.768e-18	5.973e-18 (3.035e-18)	1.231e-17 (3.704e-18)	<1.575e-17	<3.544e-18	8.222e-18 (3.403e-18)$^{\square}$
56C	<1.143e-18	4.915e-18 (8.659e-19)	<4.024e-18	7.139e-18 (1.290e-18)	<7.657e-18	5.764e-18 (1.706e-18)$^{\square\dagger}$
56D*	–	–	1.892e-17 (8.559e-19)$^{\square}$	1.338e-17 (2.767e-18)	8.456e-18 (2.124e-18)$^{\square}$	1.136e-17 (1.441e-18)$^{\square}$
56E	<3.736e-18	3.169e-18 (7.172e-19)	<1.122e-18	1.027e-18 (4.599e-19)$^{\square}$	<2.200e-18	2.641e-18 (7.172e-19)$^{\square\dagger}$
57A$^{\bullet}$	3.521e-18 (4.759e-19)	1.311e-17 (5.390e-19)	2.622e-18 (5.269e-19)	5.754e-18 (4.856e-19)	1.343e-18 (6.313e-19)$^{\square}$	2.792e-18 (6.507e-19)$^{\square\dagger}$
57A$^{\diamond}$	7.728e-18 (1.699e-18)	7.612e-17 (2.456e-19)	–	–	–	–
67B	5.306e-18 (1.044e-18)	1.800e-17 (2.793e-18)	1.036e-17 (1.655e-18)$^{\square}$	1.528e-17 (3.829e-18)$^{\square}$	2.852e-17 (4.397e-18)$^{\square}$	<2.102e-17
68A	<1.642e-18	1.212e-17 (9.984e-19)	1.037e-17 (9.887e-19)	2.026e-17 (1.115e-18)	<1.193e-17	<1.605e-17 †
68B	<1.709e-18	4.415e-18 (9.170e-19)	<2.312e-18	3.685e-18 (8.024e-19)	<3.436e-18	<7.999e-18†
68C	7.839e-18 (8.386e-19)	3.919e-17 (1.540e-18)	2.625e-17 (2.388e-18)	5.779e-17 (3.792e-18)	<1.566e-17	<2.433e-17
75D$^{\diamond}$	2.163e-18 (6.665e-19)	7.513e-18 (1.533e-18)	–	–	–	–
79A	3.830e-18 (4.552e-19)	1.248e-17 (1.053e-18)	5.138e-18 (3.508e-19)$^{\square}$	1.062e-17 (7.780e-19)	<5.298e-18	< 3.660e-18
79B	1.028e-18 (2.694e-19)	6.854e-18 (5.797e-19)	1.867e-18 (5.214e-19)$^{\square}$	2.563e-18 (7.620e-19)	<5.196e-18	1.783e-17 (2.512e-18)$^{\square}$
82B	1.684e-18 (3.707e-19)	4.619e-18 (8.734e-19)	<2.300e-18	2.644e-18 (1.024e-18)	<4.643e-18	<1.333e-18†
82C	1.026e-17 (8.441e-19)	3.333e-17 (1.375e-18)	9.751e-18 (7.786e-19)$^{\square}$	1.208e-17 (1.113e-18)	<6.353e-18	1.528e-17 (2.511e-18)$^{\square}$
91A	1.346e-17 (1.010e-18)	4.585e-17 (1.844e-18)	1.078e-17 (1.468e-18)$^{\square}$	1.831e-17 (1.662e-18)$^{\square}$	<1.186e-17	2.959e-17 (5.604e-18)$^{\square\dagger}$
91C	<2.228e-18	1.028e-17 (1.750e-18)	2.327e-18 (7.695e-19)$^{\square}$	7.423e-18 (1.079e-18)	<7.423e-18	<7.430e-18
95C	2.249e-18 (7.984e-19)	8.838e-18 (1.317e-18)	5.388e-18 (7.923e-19)	1.707e-17 (1.975e-18)	<5.144e-18	7.497e-18 (2.633e-18)
96A	3.337e-17 (2.346e-18)	5.041e-17 (3.424e-18)	5.085e-17 (1.418e-18)$^{\square}$	<3.897e-18	5.609e-17 (3.380e-18)$^{\square}$	1.472e-16 (4.225e-18)$^{\square\dagger}$
96C	2.954e-18 (9.037e-19)	1.795e-17 (1.498e-18)	7.339e-18 (8.066e-19)	1.104e-17 (1.407e-18)	<5.604e-18	1.462e-17 (3.051e-18)$^{\square}$
100A	5.569e-18 (9.621e-19)	3.240e-17 (1.723e-18)	6.564e-18 (5.994e-19)	1.662e-17 (9.197e-19)	<9.418e-18	2.584e-17 (2.536e-18)$^{\square}$

Uncertainties are listed in parentheses. Marginal detections are low signal to noise as determined by visual inspection.
† Blended with [ArII] 6.98μm
$^{\square}$ Marginal Detection
* SL coverage
$^{\diamond}$ LL coverage
$^{\bullet}$ Off nuclear extraction

TABLE A3: Observed PAH Fluxes in units of W m^{-2}

Source	6.2μm	7.7μm	8.6μm	11.3μm	12.0μm	12.6μm	17μm
6B	4.887e-17 (4.680e-18)	8.243e-17 (1.297e-17)	2.040e-17 (4.442e-18)	5.249e-17 (3.756e-18)	1.523e-17 (2.321e-18)	2.342e-17 (2.536e-18)	3.676e-17 (2.710e-18)
15A	3.540e-17 (7.305e-18)$^{\square}$	1.801e-16 (8.771e-18)	4.074e-17 (5.875e-18)	6.837e-17 (2.427e-18)	<1.070e-17	2.597e-17 (3.200e-18)	7.251e-17 (4.287e-18)
15D	<6.174e-17	2.032e-16 (2.877e-17)	<2.337e-17	6.964e-17 (5.563e-18)	1.485e-17 (6.701e-18)	<8.418e-18	2.192e-17 (7.626e-18)
25B*	7.689e-18 (7.358e-19)	3.357e-17 (1.538e-18)	6.939e-18 (5.788e-19)	1.848e-17 (1.940e-19)	7.228e-18 (2.091e-19)	9.607e-18 (1.871e-19)	–
25B$^{\diamond\bullet}$	–	–	–	–	–	–	6.379e-16 (1.166e-18)
31A+C$^{\star\bullet}$	1.365e-17 (3.994e-19)	3.780e-17 (8.320e-19)	7.066e-18 (3.023e-19)	1.278e-17 (1.103e-19)	4.095e-18 (1.370e-19)	7.486e-18 (1.484e-19)	–
31A+C$^{\diamond}$	–	–	–	–	–	–	2.376e-16 (4.624e-19)
40B	7.170e-17 (5.749e-18)$^{\square}$	6.738e-17 (7.512e-18)	1.622e-17 (4.595e-18)	4.554e-17 (3.003e-18)	<3.919e-18	1.491e-17 (4.326e-18)	<1.469e-17
40C$^{\star\bullet}$	1.319e-17 (5.119e-19)	3.887e-17 (1.208e-18)	9.010e-18 (5.650e-19)	1.555e-17 (3.918e-19)	3.898e-18 (2.845e-19)	9.877e-18 (2.920e-19)	–
40C$^{\diamond}$	–	–	–	–	–	–	1.524e-15 (2.062e-18)
40D	1.033e-15 (1.337e-17)	3.561e-15 (2.860e-17)	6.633e-16 (9.244e-18)	9.058e-16 (1.484e-17)	2.417e-16 (5.517e-18)	4.741e-16 (6.437e-18)	4.988e-16 (1.937e-17)
44A$^{\star\bullet}$	<1.051e-17	1.037e-16 (5.614e-18)$^{\square}$	2.189e-17 (1.916e-18)	3.914e-17 (4.805e-19)	1.815e-17 (6.773e-19)	9.427e-18 (3.950e-19)	–
44A$^{\diamond}$	–	–	–	–	–	–	1.857e-15 (4.175e-19)
44D	7.656e-16 (5.555e-17)	2.879e-15 (2.036e-16)	1.021e-15 (1.427e-16)	1.255e-15 (1.397e-16)	<1.529e-16	2.680e-16 (4.162e-17)	7.096e-16 (7.267e-17)
47A	3.529e-16 (2.302e-17)	7.118e-16 (6.860e-17)	9.348e-17 (2.120e-17)	3.640e-16 (1.234e-17)	1.126e-16 (1.318e-17)	1.650e-16 (1.282e-17)	1.179e-16 (1.423e-17)
55C	1.302e-16 (3.253e-18)	4.601e-16 (8.403e-18)	1.027e-16 (2.327e-18)	1.293e-16 (2.369e-18)	2.390e-17 (1.269e-18)	5.445e-17 (1.442e-18)	7.819e-17 (2.511e-18)
56B	<7.599e-17	3.457e-16 (6.633e-17)	<1.439e-17	2.538e-16 (1.399e-17)	1.972e-16 (1.630e-17)	1.330e-16 (1.568e-17)	2.918e-16 (1.856e-17)
56C	4.972e-17 (9.903e-18)	3.228e-16 (1.748e-17)	6.813e-17 (5.966e-18)	1.218e-16 (1.496e-18)	5.649e-17 (2.109e-18)	2.935e-17 (1.229e-18)	<1.666e-17
56D*	3.337e-16 (1.170e-17)	7.553e-16 (2.350e-17)	1.618e-16 (1.319e-17)	1.914e-16 (1.259e-17)	<9.407e-18	3.028e-17 (1.515e-18)	–
56E	6.294e-17 (2.653e-18)	2.540e-16 (6.618e-18)	4.730e-17 (2.157e-18)	5.496e-17 (1.055e-18)	1.294e-17 (1.323e-18)	2.286e-17 (1.447e-18)	2.499e-17 (3.501e-18)
57A$^{\bullet}$	3.918e-17 (1.651e-18)	1.433e-16 (5.967e-18)	2.508e-17 (2.045e-18)	5.307e-17 (1.507e-18)	1.823e-17 (2.041e-18)	2.444e-17 (2.253e-18)	5.068e-17 (2.757e-18)
57A$^{\diamond}$	–	–	–	–	–	–	4.564e-16 (1.887e-18)
67B	1.104e-15 (1.766e-17)	4.201e-15 (6.808e-17)	7.128e-16 (1.455e-17)	9.034e-16 (1.341e-17)	2.917e-16 (7.759e-18)	5.261e-16 (8.408e-18)	2.416e-16 (9.284e-18)
68A	1.168e-16 (5.306e-18)	<8.205e-17	<3.644e-17	1.442e-16 (2.168e-18)	3.786e-17 (3.059e-18)	3.908e-17 (3.000e-18)	9.871e-17 (4.280e-18)
68B	5.253e-17 (6.416e-18)	1.117e-16 (6.815e-18)	1.542e-17 (3.073e-18)	1.028e-16 (1.665e-18)	2.346e-17 (2.352e-18)	4.577e-17 (3.457e-18)	1.060e-16 (4.077e-18)
68C	1.045e-15 (2.108e-17)	2.964e-15 (7.289e-17)	4.906e-16 (1.552e-17)	1.046e-15 (7.681e-18)	3.649e-16 (8.636e-18)	5.015e-16 (7.960e-18)	7.284e-16 (9.992e-18)
75D$^{\diamond}$	–	–	–	–	–	–	1.844e-16 (2.583e-17)
79A	6.546e-16 (5.593e-18)	2.483e-15 (1.268e-17)	3.424e-16 (3.394e-18)	4.291e-16 (2.668e-18)	1.281e-16 (2.033e-18)	2.652e-16 (1.990e-18)	2.608e-16 (6.256e-18)
79B	2.760e-16 (6.515e-18)	9.979e-16 (2.698e-17)	1.606e-16 (3.098e-18)	2.040e-16 (4.496e-18)	7.498e-17 (2.311e-18)	1.327e-16 (2.878e-18)	9.559e-17 (4.119e-18)
82B	4.659e-17 (5.080e-18)	1.977e-16 (1.941e-17)	3.197e-17 (3.731e-18)	5.797e-17 (2.708e-18)	9.219e-18 (2.504e-18)	2.647e-17 (2.714e-18)	4.386e-17 (5.425e-18)
82C	1.157e-15 (9.503e-18)	4.116e-15 (2.664e-17)	6.894e-16 (7.531e-18)	7.082e-16 (7.277e-18)	2.260e-16 (3.150e-18)	4.615e-16 (3.427e-18)	4.445e-16 (1.119e-17)
91A	7.837e-16 (1.712e-17)	1.996e-15 (5.703e-17)	2.009e-16 (7.835e-18)	6.046e-16 (4.341e-18)	1.983e-16 (5.965e-18)	2.840e-16 (6.344e-18)	6.052e-16 (8.812e-18)
91C	3.142e-16 (7.112e-18)	1.098e-15 (2.869e-17)	2.135e-16 (5.177e-18)	2.488e-16 (3.136e-18)	6.280e-17 (3.899e-18)	1.510e-16 (4.302e-18)	1.586e-16 (9.371e-18)
95C	1.081e-16 (8.582e-18)	4.714e-16 (2.685e-17)	9.415e-17 (4.675e-18)	1.364e-16 (4.887e-18)	4.481e-17 (3.553e-18)	8.102e-17 (3.839e-18)	1.477e-16 (1.020e-17)
96A	2.593e-15 (1.179e-17)	1.197e-14 (4.933e-17)	7.595e-16 (8.759e-18)	1.736e-15 (4.418e-18)	1.007e-15 (6.902e-18)	1.410e-15 (6.369e-18)	2.030e-15 (2.042e-17)
96C	7.005e-16 (1.056e-17)	2.209e-15 (3.928e-17)	4.341e-16 (7.732e-18)	5.684e-16 (1.190e-17)	1.558e-16 (4.062e-18)	2.825e-16 (4.642e-18)	2.439e-16 (1.070e-17)
100A	1.226e-15 (7.659e-18)	4.220e-15 (2.289e-17)	6.740e-16 (3.410e-18)	1.209e-15 (2.044e-18)	2.752e-16 (2.881e-18)	6.563e-16 (3.496e-18)	6.432e-16 (7.450e-18)

Uncertainties are listed in parentheses. Marginal detections are low signal to noise as determined by visual inspection.
$^{\square}$ Marginal Detection
* SL coverage
$^{\diamond}$ LL coverage
$^{\bullet}$ Off nuclear extraction

TABLE A4: Observed Forbidden Line Fluxes in units of W m^{-2}

Source	[ArII] 6.98μm	[NeII] 12.81μm	[NeIII] 15.56μm	[SIII] 18.71μm	[OIV] 25.89μm/ [FeII] 25.98μm	[SIII] 33.48μm	[SiII] 34.82μm
6B	<3.400e-18†	1.364e-18 (4.693e-19)$^{\square}$	2.568e-18 (4.584e-19)$^{\square}$	<1.306e-18	1.575e-18 (4.075e-19)	<3.423e-18	3.674e-18 (1.066e-18)
15A	5.290e-18 (1.470e-18)	2.452e-18 (6.782e-19)	6.353e-18 (7.423e-19)	4.737e-18 (7.139e-19)	<2.554e-18	<4.0479e-18	1.033e-17 (2.001e-18)
15D	<1.072e-17†	4.369e-18 (1.704e-18)$^{\square}$	<4.799e-18	<3.546e-18	<6.896e-18	<3.141e-18	4.005e-18 (1.893e-18)$^{\square}$
25B*	9.752e-19 (2.419e-19)$^{\square\dagger}$	5.534e-19 (4.702e-20)	–	–	–	–	–
25B$^{\diamond\bullet}$	–	–	1.772e-18 (1.979e-20)	<4.689e-18	<2.629e-18	<4.047e-18	<4.604e-18
31A+C$^{\diamond}$	–	–	3.737e-16 (6.930e-20)	2.718e-16 (1.148e-19)	<1.690e-17	2.786e-16 (1.446e-17)	1.269e-16 (1.366e-17)
40B	<3.457e-18	3.542e-18 (1.002e-18)$^{\square}$	3.353e-18 (1.045e-18)$^{\square}$	<2.196e-18	3.748e-18 (6.926e-19)$^{\square}$	<3.748e-18	<7.405e-18
40C$^{\star\bullet}$	4.938e-19 (1.332e-19)$^{\square\dagger}$	5.706e-19 (7.023e-20)	–	–	–	–	–
40C$^{\diamond}$	–	–	2.452e-17 (2.294e-20)	8.971e-17 (1.469e-19)	3.861e-18 (1.208e-18)	6.325e-17 (1.651e-20)	1.602e-16 (2.331e-20)
40D	5.886e-17 (2.446e-18)	1.114e-16 (1.431e-18)	8.048e-18 (1.824e-18)	3.385e-17 (2.402e-18)	1.365e-17 (1.376e-18)	4.870e-17 (5.056e-18)	1.190e-16 (4.805e-18)
44A$^{\star\bullet}$	2.621e-18 (8.208e-19)$^{\square}$	1.849e-18 (2.263e-19)	–	–	–	–	–
44A$^{\diamond}$	–	–	5.692e-17 (1.718e-20)	3.348e-17 (4.615e-20)	2.096e-17 (9.390e-18)	3.348e-17 (7.745e-18)	1.863e-16 (6.930e-18)$^{\square}$
44D	4.933e-17 (1.245e-17)$^{\square\dagger}$	4.149e-17 (8.400e-18)	5.717e-17 (7.080e-18)	1.540e-16 (1.346e-17)	7.843e-18 (3.406e-18)	9.845e-17 (5.490e-18)	8.545e-17 (5.903e-18)
47A	3.295e-17 (5.367e-18)$^{\square\dagger}$	3.745e-17 (3.049e-18)	5.792e-18 (2.624e-18)	1.928e-17 (2.403e-18)	<9.792e-18	4.433e-17 (2.369e-18)	4.356e-17 (2.998e-18)
55C	<5.808e-18†	1.002e-17 (2.574e-19)	2.021e-18 (4.941e-19)	3.873e-18 (7.648e-19)	<1.045e-18	6.434e-18 (4.134e-19)	1.487e-17 (7.770e-19)
56B	2.725e-17 (4.189e-18)	3.636e-17 (4.169e-18)	6.748e-17 (3.365e-18)	1.813e-17 (2.695e-18)	8.377e-17 (2.220e-18)	1.377e-17 (2.569e-18)	1.610e-17 (3.423e-18)
56C	8.005e-18 (1.469e-18)$^{\square\dagger}$	4.830e-18 (1.316e-18)$^{\square}$	2.555e-18 (9.593e-19)$^{\square}$	2.581e-18 (5.985e-19)$^{\square}$	<4.609e-18	6.053e-18 (1.783e-18)$^{\square}$	<7.828e-18
56D*	3.089e-17 (1.583e-18)	2.381e-17 (8.803e-19)	–	–	–	–	–
56E	3.111e-18 (7.657e-19)$^{\square\dagger}$	5.185e-18 (3.979e-19)	1.682e-18 (4.357e-19)	4.846e-18 (5.428e-19)	<2.224e-18	5.767e-18 (1.502e-18)	2.559e-18 (1.575e-18)
57A$^{\bullet}$	1.216e-18 (5.026e-19)$^{\square\dagger}$	4.006e-18 (5.876e-19)	3.084e-18 (5.026e-19)	1.585e-18 (3.229e-19)	1.148e-18 (5.099e-19)	2.719e-18 (7.600e-19)	4.637e-18 (8.110e-19)
57A$^{\diamond}$	–	–	1.184e-17 (2.592e-20)	3.971e-18 (7.379e-20)	<1.875e-18	1.010e-17 (2.515e-18)	2.845e-17 (2.864e-18)
67B	4.092e-17 (7.869e-18)	7.530e-17 (1.715e-18)	3.404e-18 (1.672e-18)$^{\square}$	8.065e-18 (1.426e-18)	<5.662e-18	1.825e-17 (2.334e-18)	5.212e-17 (3.192e-18)
68A	1.706e-17 (2.472e-18)$^{\square\dagger}$	1.270e-17 (7.531e-19)	1.435e-17 (7.590e-19)	6.979e-18 (9.325e-19)	4.381e-18 (5.709e-19)	6.465e-18 (1.202e-18)	1.774e-17 (1.338e-18)
68B	4.644e-18 (2.089e-18)$^{\square\dagger}$	3.880e-18 (6.767e-19)	1.206e-17 (6.631e-19)	5.383e-18 (7.310e-19)	<3.986e-18	2.921e-18 (8.830e-19)$^{\square}$	8.915e-18 (1.155e-18)$^{\square}$
68C	9.516e-17 (7.711e-18)	1.207e-16 (2.188e-18)	2.078e-17 (1.134e-18)	3.974e-17 (1.464e-18)	8.149e-18 (9.425e-19)	3.573e-17 (1.721e-18)	7.328e-17 (1.969e-18)
75D$^{\diamond}$	–	–	<1.730e-18	1.666e-17 (2.527e-18)	1.763e-18 (7.331e-19)	1.309e-17 (1.569e-18)	2.460e-17 (1.939e-18)
79A	2.106e-17 (1.427e-18)	3.949e-17 (4.816e-19)	7.949e-18 (6.939e-19)	1.639e-17 (9.172e-19)	2.293e-18 (4.442e-19)	3.040e-17 (1.113e-18)	5.215e-17 (1.384e-18)
79B	9.151e-18 (2.436e-18)	2.363e-17 (5.177e-19)	4.156e-18 (3.445e-19)	9.698e-18 (6.162e-19)	3.719e-18 (3.252e-19)	1.371e-17 (6.089e-19)	2.767e-17 (8.313e-19)
82B	<4.450e-18†	4.770e-18 (6.114e-19)	3.503e-18 (6.453e-19)	5.095e-18 (8.831e-19)	<1.618e-18	2.829e-18 (1.058e-18)$^{\square}$	4.949e-18 (1.271e-18)$^{\square}$
82C	5.974e-17 (2.780e-18)	1.179e-16 (9.169e-19)	1.921e-17 (1.077e-18)	3.471e-17 (2.088e-18)	8.369e-18 (2.263e-18)	6.899e-17 (1.761e-18)	9.751e-17 (3.246e-18)
91A	3.796e-17 (5.058e-18)$^{\square\dagger}$	5.676e-17 (1.286e-18)	2.693e-17 (1.504e-18)	4.185e-17 (1.468e-18)	2.474e-17 (3.857e-18)	5.955e-17 (2.402e-18)	1.261e-16 (2.511e-18)
91C	1.376e-17 (3.007e-18)	2.140e-17 (9.767e-19)	3.949e-18 (1.580e-18)	1.469e-17 (2.013e-18)	<7.169e-18	1.418e-17 (2.166e-18)	4.348e-17 (3.185e-18)
95C	6.705e-18 (3.206e-18)	1.481e-17 (7.070e-19)	6.089e-18 (1.085e-18)	9.996e-18 (1.201e-18)	1.792e-18 (7.802e-19)	1.195e-17 (1.268e-18)	1.664e-17 (1.810e-18)
96A	7.912e-17 (4.590e-18)$^{\square\dagger}$	2.506e-16 (1.260e-18)	2.448e-16 (2.681e-18)	1.544e-16 (2.346e-18)	3.031e-16 (1.923e-18)	2.506e-16 (3.744e-18)	1.661e-16 (4.866e-18)
96C	2.650e-17 (3.245e-18)	5.489e-17 (1.007e-18)	1.274e-17 (1.225e-18)	1.528e-17 (1.322e-18)	4.755e-18 (1.134e-18)	2.638e-17 (2.117e-18)	4.719e-17 (2.942e-18)
100A	6.115e-17 (2.560e-18)	1.080e-16 (7.013e-19)	2.548e-17 (1.359e-18)	9.609e-17 (1.274e-18)	1.003e-17 (1.614e-18)	1.164e-16 (2.293e-18)	1.359e-16 (2.269e-18)

Uncertainties are listed in parentheses. Marginal detections are low signal to noise lines as determined by visual inspection.
† Blended with H_2 S(5) 6.91μm
$^{\square}$ Marginal Detection
* SL coverage
$^{\diamond}$ LL coverage
$^{\bullet}$ Off-nuclear extraction

TABLE A5: H_2-detected Extraction Areas

Galaxy	SL Area (arcsec^2)	LL Area (arcsec^2)	SF[a]
6B	27.3	154.8	1
15A	75.3	309.6	1
15D	47.9	309.8	2.50
25B	82.3	–	
25B•	–	516.5	
31A+C	–	722.7	
31A+C•	82.3	–	
40B	47.8	258.5	3.37
40C	–	516.5	
40C•	77.8	–	
40D	95.6	464.6	1.96
44A	–	619.4	
44A•	116.0	–	
44D	93.5	878.1	5.90
47A	75.0	361.3	3.79
55C	68.4	258.2	1
56B	61.9	412.5	1.59
56C	54.7	361.2	4.09
56D	54.8	–	
56E	41.0	206.2	1
57A	–	413.1	
57A•	67.9	103.3	1
67B	170.4	361.2	1
68A	61.7	412.4	5.33
68B	75.4	361.2	1
68C	308.6	775.6	2.24
75D	–	257.8	
79A	61.6	361.3	1.58
79B	68.6	155.1	1.24
82B	34.3	206.4	1
82C	54.7	309.6	1.60
91A	225.1	516.0	1.53
91C	47.8	361.3	2.36
95C	82.7	259.3	1
96A	130.9	619.9	1.64
96C	41.4	258.0	1.61
100A	68.4	516.2	1

[a] Scale Factor
• Off-nuclear extraction

The HCG 31A+C complex (Fig. B1a and b) has an irregular morphology and high levels of star formation; it is likely experiencing a triggered starburst due to the mutual interaction between the two parent systems (Gallagher et al. 2010). HCG 91A appears strongly star forming (Fig. B2d), but has an optically-identified active nucleus (Sy1.2, Radovich et al. 1998); we note our extraction is optimised to include the disk.

If we consider the morphological types of the non-MOHEG H_2 galaxies listed in Table 3, many are classified as peculiar early type galaxies (Sa or S0). However, these galaxies have spectra consistent with current star formation (strong PAH emission and a sharply rising mid-infrared continuum). Bitsakis et al. (2011) have suggested that several systems are misclassified (due to orientation and dust obscuration). For the galaxies 55C, 56D and 56E (see Fig. B1) our spectra don't rule out this possibility, as proposed by Bitsakis et al. (2011), based on their SEDs and IRAC mid-infrared morphology. In addition, their global mid-infrared colors are consistent with late type systems ($\log[f_{5.8\mu m}/f_{3.6\mu m}] > 0$) and their nuclear classifications suggest they are star-forming systems (Coziol et al. 2004).

HCG 79A has a star-forming spectrum (Fig. B2a), but a mid-infrared color of $\log[f_{5.8\mu m}/f_{3.6\mu m}]$ = -0.06, i.e. at the blue end of the mid-infrared green valley. Inspection of its IRAC image (included as Figure B3a) suggests that 79A is an S0/a type. The star formation seen in its spectrum could be the result of a minor merger or gas accretion that has introduced fuel for star formation and is expected to further build the lenticular bulge (Shapiro et al. 2010). The Hα velocity field determined by Durbala et al. (2008) suggests a cross-fueling (discrete infall or fueling event rather than a continuous flow) from HCG 79D. Evidence for a minor merger in HCG 79A was also seen by Coziol & Plauchu-Frayn (2007) based on the asymmetry observed in their near-infrared images.

Within our sample, Bitsakis et al. (2011) have also suggested 79B and 100A are late type galaxies misclassified as early types. Inspection of their spectra indicates star formation is occurring (Figures B2b and B2h, respectively). We note that their SEDs (Bitsakis et al. 2011) indicate the presence of a warm dust continuum superimposed on a substantial stellar component. However, we draw attention to these galaxies since they have IRAC colors ($\log[f_{5.8\mu m}/f_{3.6\mu m}]$) of -0.18 and -0.05, for HCG 79B and 100A, respectively. This places them at intermediate mid-infrared color. We show these galaxies in Figure B3a and B3b, respectively, and draw attention to their disturbed morphologies. HCG 79B displays a magnificent tidal feature and there is evidence that it has accreted a dwarf (Durbala et al. 2008). These galaxies are all classified as early type disk systems (S0/a), but we may be seeing the effect of minor mergers or gas

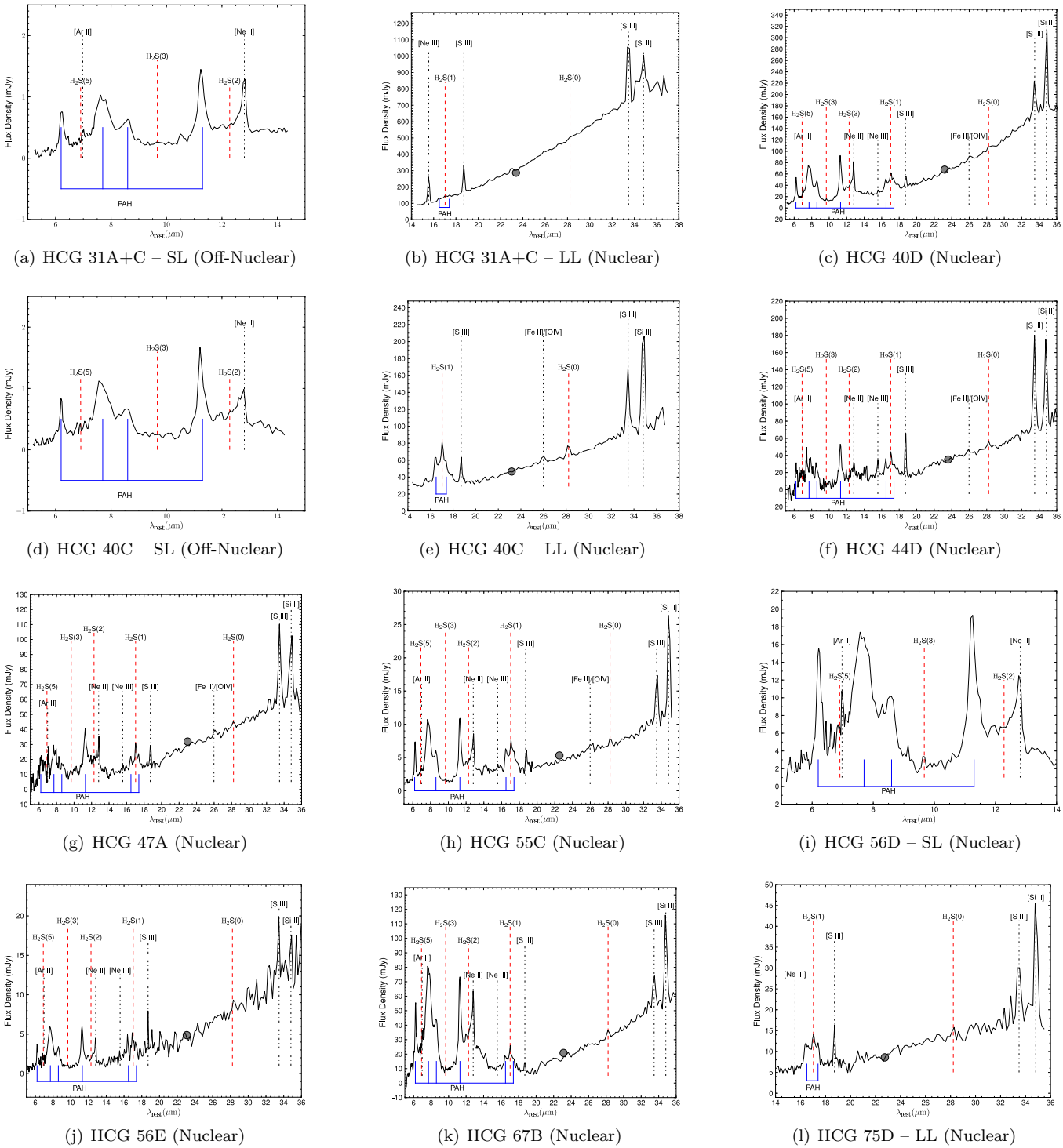

(a) HCG 31A+C – SL (Off-Nuclear)
(b) HCG 31A+C – LL (Nuclear)
(c) HCG 40D (Nuclear)
(d) HCG 40C – SL (Off-Nuclear)
(e) HCG 40C – LL (Nuclear)
(f) HCG 44D (Nuclear)
(g) HCG 47A (Nuclear)
(h) HCG 55C (Nuclear)
(i) HCG 56D – SL (Nuclear)
(j) HCG 56E (Nuclear)
(k) HCG 67B (Nuclear)
(l) HCG 75D – LL (Nuclear)

FIG. B1: Non-MOHEG, H_2-detected HCG Galaxies. The matched MIPS 24μm photometry is shown as a grey point.

accretion producing star formation and giving rise to the combination of relatively dusty mid-infrared colours with mid-infrared spectra indicative of star formation. Alternatively star formation is being actively shut off or "starved" by some mechanism. It is therefore not clear that these galaxies are misclassifications.

C. H_2 UPPER LIMITS FOR NON-DETECTIONS IN THE REST OF THE SAMPLE

In this section we give the H_2 upper limits for the S(0), S(1), S(2) and S(3) lines (Table C1) and measured PAH values and upper limits for galaxies in the sample with an extracted spectrum (Table C2.

As noted in the text, several galaxies with star-forming, mid-infrared colours do not have detected H_2 emission. In

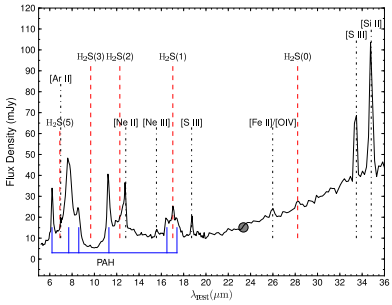

(a) HCG 79A (Nuclear)

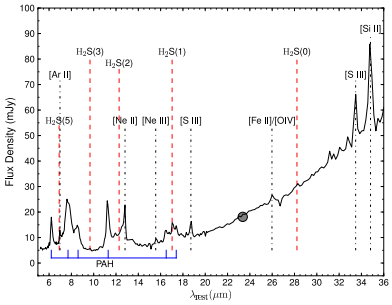

(b) HCG 79B (Nuclear)

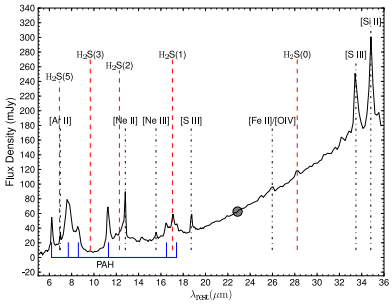

(c) HCG 82C (Nuclear)

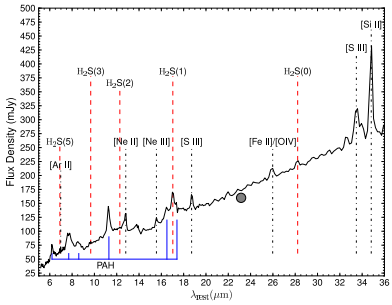

(d) HCG 91A (Nuclear)

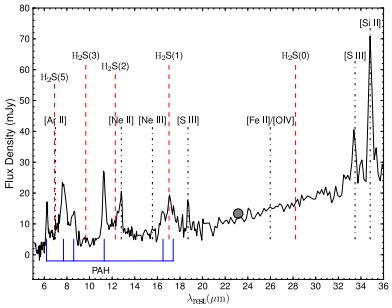

(e) HCG 91C (Nuclear)

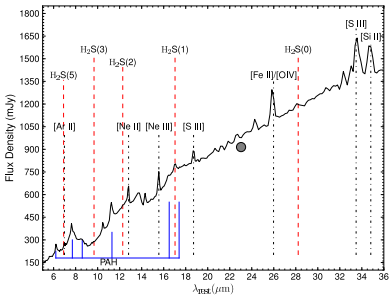

(f) HCG 96A (Nuclear)

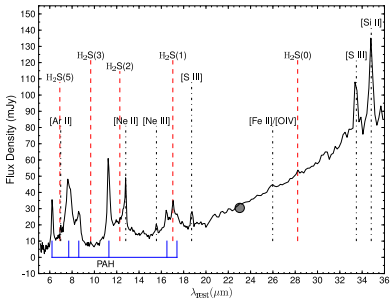

(g) HCG 96C (Nuclear)

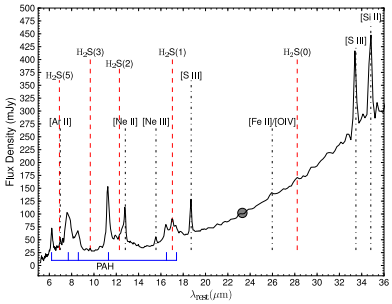

(h) HCG 100A (Nuclear)

FIG. B2: Non-MOHEG, H_2-detected HCG Galaxies. The matched MIPS 24μm photometry is shown as a grey point.

Figure C1a we use HCG 31B to illustrate the typical spectrum of these systems. Excited H_2 emission is associated with PDRs in star-forming galaxies (Hollenbach & Tielens 1997). However, given the large aperture (the LL slit coverage is shown in Figure C1b) of our extractions, which include the nuclear and disk regions, and depending on the geometry of dust and star forming regions, the H_2 line contrast can be effected by the warm dust continuum which may dominate entirely. This is less of an effect when targeting the nuclei and H II regions of nearby galaxies (see, for example, Roussel et al. 2007), but a feature of our study since our observations are tailored to finding IGM detections of excited H_2, where continuum levels are low, and shock-driven H_2, which have been shown to be a powerful cooling channel (see, for example, Cluver et al. 2010).

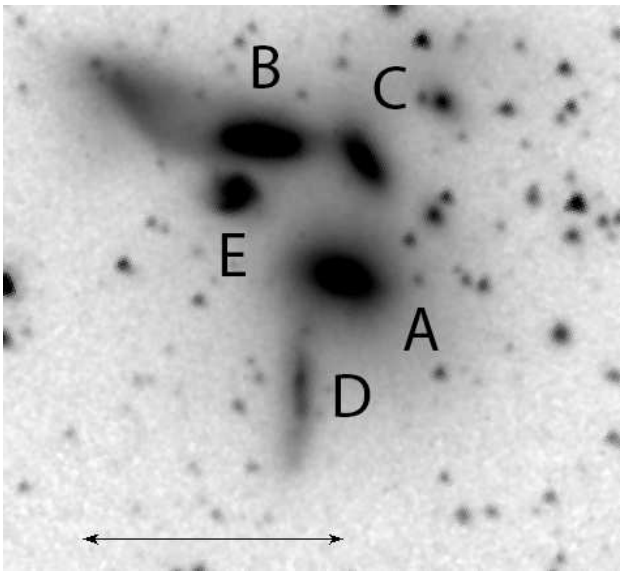

(a) 79A and 79B

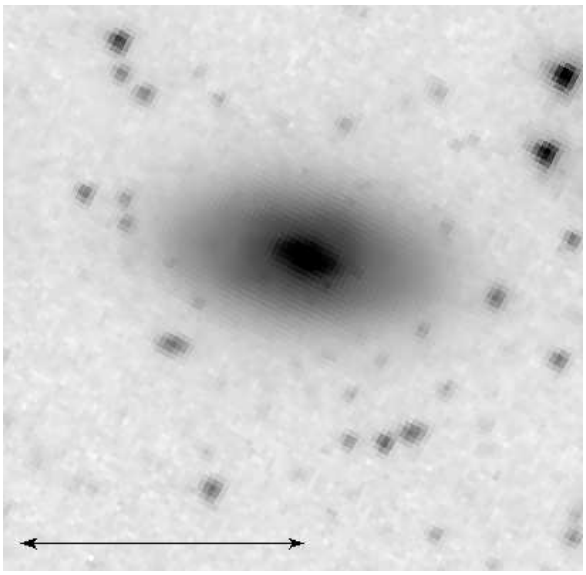

(b) 100A

FIG. B3: IRAC 3.6μm images of the non-MOHEG H_2-detected galaxies which lie within the green valley; the arrow is 1′ in length. These systems all have spectra that indicate active star formation.

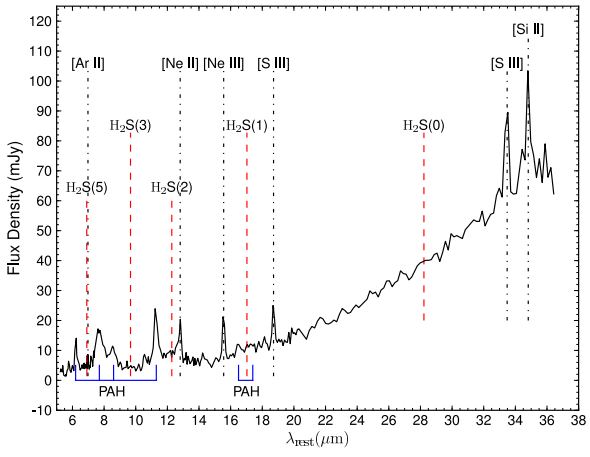

(a) 31B

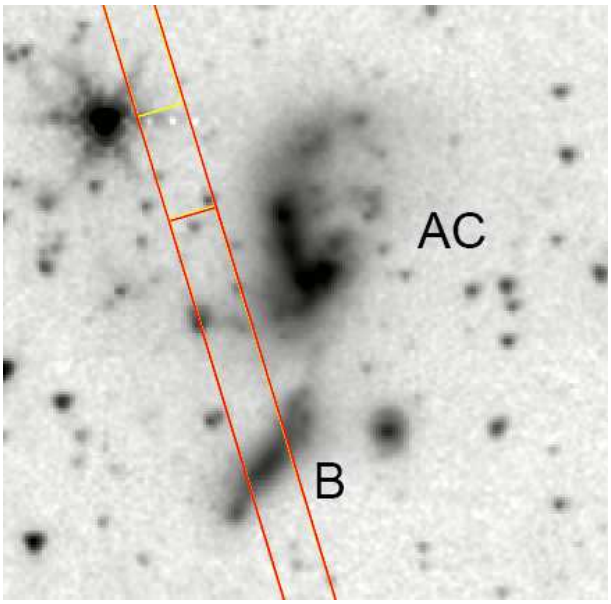

(b) LL slit on an IRAC 3.6μm image (2′×2′)

FIG. C1: a) The spectrum of HCG 31B is shown as typical of galaxies with star-forming mid-infrared colours, but no H_2 detections. b) Here the LL slit overlay shows that the coverage for the galaxy includes the nuclear and much of the disk region, thus the spectrum in (a) is broadly representative of the galaxy's global properties.

TABLE C1: H_2 Upper Limits for the Remainder of Sample in units of $W\,m^{-2}$

Galaxy	H_2 0-0 S(0) $\lambda 28.21\mu$m	H_2 0-0 S(1) $\lambda 17.03\mu$m	H_2 0-0 S(2) $\lambda 12.28\mu$m	H_2 0-0 S(3) $\lambda 9.66\mu$m
8A	<1.513e-18	<2.286e-18	<5.699e-19	<1.142e-18
8C	<1.897e-18	<2.509e-18	<7.261e-19	<1.566e-18
8D	<1.752e-18	<3.618e-18	<1.298e-18	<1.592e-18
15C	<1.506e-18	<3.299e-18	<1.196e-18	<2.198e-18
25D	<1.650e-18	<2.958e-18	<1.161e-18	<1.252e-18
25F	<1.864e-18	<3.186e-18	<9.264e-19	<1.825e-18
40A	<1.415e-18	<2.303e-18	<7.692e-19	<1.173e-18
31B	< 2.864e-18	< 2.383e-18	< 3.292e-18	< 4.508e-18
44B	<1.976e-18	<3.267e-18	<1.883e-18	<6.087e-18
47B	<1.284e-18	<1.454e-18	<1.342e-18	<2.156e-18
47D	<4.018e-18	<5.080e-18	<3.122e-18	<3.052e-18
54A	<1.415e-18	<4.105e-18	<1.108e-18	<2.264e-18
54B	<2.152e-18	<2.184e-18	<2.537e-18	<6.094e-18
54C	<1.564e-18	<2.643e-18	<8.198e-19	<1.662e-18
55A	<7.940e-19	<9.644e-19	<3.727e-19	<5.379e-19
55B*	–	–	<6.945e-19	<5.913e-19
55D*	–	–	<2.814e-19	<4.005e-19
57B$^\diamond$	<1.108e-18	<2.865e-18	–	–
57B*	–	–	<1.709e-19	<1.994e-19
57C	<1.945e-18	<2.728e-18	–	–
57D	<2.085e-18	–	–	–
57E	<1.361e-18	<2.108e-18	<6.653e-19	<9.469e-19
62A$^\diamond$	<9.610e-19	<1.881e-18	–	–
62A*	–	–	<1.776e-18	<3.169e-18
62B	<1.082e-18	<1.588e-18	<1.578e-18	<3.723e-18
62C	<9.707e-19	<1.422e-18	<9.435e-19	<2.819e-18
67A	<2.099e-18	<3.888e-18	<4.141e-18	<7.609e-18
67D	<1.704e-18	<2.371e-18	–	–
75A	<2.375e-18	<2.323e-18	<2.861e-18	<6.098e-18
75C	<9.559e-19	<1.815e-18	<1.804e-18	<2.296e-18
75E	<1.333e-18	<1.768e-18	<6.877e-19	<1.205e-18
82A	<1.331e-18	<2.363e-18	<3.547e-19	<7.162e-19
91D	<2.280e-18	<5.068e-18	<5.111e-19	<1.894e-18
95A	<1.506e-18	<2.906e-18	<1.561e-18	<3.768e-18
96B	<1.241e-18	<3.459e-18	<1.041e-18	<2.242e-18
97A	<1.798e-18	<2.312e-18	<1.042e-18	<1.490e-18
97C	<1.510e-18	<3.099e-18	<1.357e-18	<2.160e-18
97D	<1.988e-18	<2.146e-18	<1.450e-18	<3.818e-18
100B	<2.716e-18	<5.954e-18	<1.867e-18	<4.176e-18
100C	<1.965e-18	<3.052e-18	<1.643e-18	<2.809e-18

* SL coverage only
$^\diamond$ LL coverage only

TABLE C2: Measurements for Main PAH features for Remainder of Sample in units of $\mathrm{W\,m^{-2}}$

Galaxy	6.2μm	7.7μm	11.3μm
8A	<6.014e-18	<7.630e-18	9.170e-18 (1.826e-18)
8C	<7.029e-18	<7.961e-17	1.754e-17 (2.363e-18)
8D	<7.180e-18	5.434e-17 (4.884e-18)	2.076e-17 (8.858e-19)
15C	<1.788e-17	<5.850e-17	<5.884e-18
25D	<7.194e-18	<2.707e-17	<4.555e-18
25F	<4.319e-18	<3.667e-17	<2.530e-18
31B	2.269e-16 (1.306e-17)	6.022e-16 (5.166e-17)	2.119e-16 (6.787e-18)
40A	<7.947e-18	1.058e-17 (2.645e-18)	1.242e-17 (5.437e-19)
44B	<1.912e-17	<1.127e-16	<9.197e-18
47B	<1.214e-17	<6.908e-17	<6.273e-18
47D	<4.196e-17	<4.482e-17	2.309e-17 (3.805e-18)
54A	<1.180e-17	6.653e-17 (6.314e-18)	1.318e-17 (1.314e-18)
54B	9.182e-17 (9.197e-18)	1.764e-16 (1.756e-17)	6.839e-17 (7.564e-18)
54C	<8.366e-18	6.307e-17 (6.260e-18)	1.568e-17 (2.409e-18)
55A	<9.556e-18	<7.376e-18	1.248e-18 (3.539e-19)
55B	<4.214e-18	<1.768e-17	<1.422e-18
55D	<2.492e-18	<4.115e-18	2.180e-18 (6.428e-19)
57B	<3.270e-18	4.168e-18 (1.015e-18)	2.027e-18 (3.227e-19)
57C$^{\diamond}$	–	–	–
57D$^{\diamond}$	–	–	–
57E	<5.498e-18	<7.503e-17	1.541e-17 (3.929e-18)
62A	3.606e-17 (7.201e-18)	< 6.775e-17	8.293e-18 (2.755e-18)
62B	<1.723e-17	<6.527e-17	<1.132e-17
62C	<1.735e-17	< 9.991e-17	<4.573e-18
67A	<5.361e-17	< 1.850e-16	<2.205e-17
67D$^{\diamond}$	–	–	–
75A	<2.737e-17	3.330e-17 (6.426e-18)	2.916e-17 (1.506e-18)
75C	2.154e-17 (6.270e-18)	8.114e-17 (2.569e-17)	3.254e-17 (2.010e-18)
75E	<2.183e-17	<1.652e-17	<6.830e-18
82A	<6.455e-18	<4.775e-17	<2.735e-18
91D	<1.781e-17	3.659e-17 (7.704e-18)	7.828e-18 (2.189e-18)
95A	<2.470e-17	<2.100e-17	<6.839e-18
96B	<1.568e-17	<7.431e-17	<4.826e-18
97A	<1.236e-17	<8.951e-17	<5.459e-18
97C	<1.510e-17	<2.646e-17	<2.602e-18
97D	<2.322e-17	<1.220e-16	<6.714e-18
100B	2.164e-16 (9.738e-18)	5.821e-16 (4.674e-17)	1.361e-16 (7.608e-18)
100C	1.999e-17 (7.049e-18)	5.320e-17 (8.919e-18)	2.929e-17 (2.515e-18)

$^{\diamond}$ LL coverage only

D. X-RAY AND RADIO PROPERTIES OF THE HCG SAMPLE

The X-ray distribution and luminosity in our HCG MOHEGs is an important consideration since XDRs (X-ray dominated regions) associated with AGN may excite H_2. It is therefore necessary to rule out photo-heating of H_2 from within the galaxies.

D.1. *Diffuse X-ray Emission from Intragroup Gas*

First we consider the amount and distribution of X-ray emission (including diffuse plasma) in the MOHEG groups to explore any connections to the H_2-enhanced systems. We have X-rays detected in 5 groups and we list the diffuse X-ray measurements obtained from the literature in Table D1. The MOHEGs HCG 15A and D appear to have some X-ray structure associated with them, in particular HCG 15D appears connected to 15F (Rasmussen et al. 2008). In HCG 40, B is H_2-enhanced, but the strongest X-ray sources are C and D, which are only H_2-detected systems and not MOHEGs (Rasmussen et al. 2008). However, HCG 40B and C appear connected in X-ray emission, particularly interesting since we detect H_2 outside 40C (see section 4.1.1). In HCG 68, the map of Forbes et al. (2006) indicates emission around MOHEGs HCG 68A and C show emission and it appears that the emission from A connects to B (also a MOHEG).

TABLE D1: Diffuse X-ray emission in MOHEG Compact Groups

Group	MOHEGs	X-ray Luminosity L_X (erg s^{-1})	$L_\odot$
HCG 6	1	$<2.7\times10^{41}$ (3σ, a)	$<7.0\times10^{7}$
HCG 15	2	$3.2\pm0.2\times10^{41}$ (b)	8.3×10^{7}
HCG 25	1	–	–
HCG 40	1	$3.1\pm0.5\times10^{40}$ (b)	8.1×10^{6}
HCG 56	1	$<1.7\times10^{42}$ (3σ, a)	$<4.4\times10^{8}$
HCG 57	1	$8.3+3.2-3.5\times10^{41}$ (c)	2.2×10^{8}
HCG 68	3	$3.3\pm0.3\times10^{41}$ (d)	8.6×10^{7}
HCG 82	1	$1.9\pm0.8\times10^{42}$ (a)	4.9×10^{8}
HCG 95	1	$<2.7\times10^{42}$ (3σ, a)	$<7.0\times10^{8}$

(a) From Ponman et al. (1996)
(b) From Rasmussen et al. (2008)
(c) From Mulchaey et al. (2003)
(d) From Osmond & Ponman (2004)

Unlike SQ, X-ray emission from a shock-front is not clearly distinguishable from the diffuse emission in the groups. SQ is, of course, notable due to the high relative velocity (~ 1000 km/s) of the collision of the intruder with the intragroup H I. Collisions of the group galaxies with tidal material would be occurring at far lower relative velocities ($100 - 1000$ km/s), thus the kinetic energy would be far less compared to SQ, resulting in weaker X-ray emission.

D.2. *X-ray Emission within Group Members*

Several galaxies appear to have nuclear enhancements in their X-ray data. Searching the archives for suitable coverage of the HCG MOHEGs, we have determined that HCG 6B, 25B, 82B and 95C have not been covered by *Chandra/XMM* and were not detected by *ROSAT*. All other available measurements (from the literature and data, as specified) are listed in Table D2. We include the radius of the measurement and the luminosity of the H_2 in relation to the X-ray. In addition, archival radio data is presented. The galaxies are listed in order of decreasing $H_2/7.7\mu$m PAH.

H_2 heating by X-rays via photoelectrons in XDR models leads to $\sim$2% of the total gas cooling via the pure rotational lines of H_2 (Maloney et al. 1996). Assuming all of the X-ray flux is absorbed by an XDR, the maximum $L(H_2$ 0-0 S(0)-S(3))$/L_X$(2-10 keV) ratio is 0.01 (Ogle et al. 2010). Assuming a power-law spectrum typical of an AGN (as in Ogle et al. 2010), we scale the fluxes in the energy bands listed in Table D2 to the L_X(2-10 keV) band. Given that our IRS spectra have only sampled a fraction of the HCG galaxies, we do not have a measure of the total amount of warm H_2 and hence the L_{H_2}/L_X values are lower limits, but still illustrative. We note that all the HCG MOHEGS have $L_{H_2}/L_X > 0.01$, usually having H_2 luminosities more than an order of magnitude greater than what can be generated by X-rays (except HCG 15D, although this measurement is contaminated by diffuse emission). We can thus rule out XDRs as being responsible for the enhanced H_2 seen in the HCG MOHEGs. This is not unexpected as even though HCG galaxies have increased AGN activity (likely due to tidal interactions), they are dominated by low luminosity AGN due to low accretion rates.

Archival radio data is also included in Table D2. The highest 1.4 GHz luminosity is associated with the Seyfert 2 galaxy HCG 56B, a candidate MOHEG for jet-ISM interactions producing the excited H_2 (see Ogle et al. 2010).

TABLE D2: MOHEG Nuclear X-ray and Radio Data

	X-ray Luminosity				Radio Data			
	L_X ($erg\,s^{-1}$)	Radius	L_X ($L_\odot$)	L_{H_2}/L_X †		$F_{1.4GHz}$ (mJy)	$L_{1.4GHz}$ ($erg\,s^{-1}$)	$\log L_{1.4GHz}$ [$W\,Hz^{-1}$]
68A	1.6×10^{40} [a,b]	4.7″	4.1×10^{6}	>0.53	NVSS◇	40.5 (1.3)	8.7×10^{37}	21.6
6B	–	–	–	–	–			
57A	4.1×10^{39} [c,d]	15″	1.1×10^{6}	>28.9	–			
40B	1.8×10^{39} [c,e]	2.1″	4.7×10^{5}	>2.42	–			
25B	–	–	–	–	–			
15D	$6.7\times10^{41}(\star)$ [c,e]	25″	1.7×10^{8}	>0.03	NVSS	4.6 (0.5)	6.6×10^{37}	21.7
68B	9.0×10^{39} [a,b]	2.3″	2.3×10^{6}	>0.18	NVSS	8.0 (0.5)	1.7×10^{37}	21.1
95C	–	–	–	–	–			
15A	$2.6\times10^{40}(\star)$ [c,e]	25″	6.8×10^{6}	>0.22	NVSS	3.6 (0.6)	5.1×10^{37}	21.6
56B	$<1.5\times10^{40}$ [c,f]	3″	$<3.8\times10^{6}$	>1.42	NVSS	26.7 (1.2)	6.1×10^{38}	22.6
68C	6.9×10^{39} [a,b]	1.2″	1.8×10^{6}	>3.70	NVSS	16.8 (1.7)	3.6×10^{37}	21.4
82B	–	–	–	–	–			
56C	$<1.5\times10^{40}$ [c,f]	3″	$<3.8\times10^{6}$	>1.69	–			

† $L(H_2\ 0\text{-}0\ S(0)\text{-}S(3))/L_X(2\text{-}10\ keV)$
◇ NRAO VLA Sky Survey; Condon et al. (1998)
($\star$) *XMM* – Can't discern point-like from diffuse emission
[a] 0.5-7 keV
[b] From Chandra Source Catalogue; Evans et al. (2010)
[c] 0.3-2 keV
[d] Derived from *XMM* pn data
[e] From Rasmussen et al. (2008)
[f] Upper limit: not detected in Chandra Source Catalogue